



## Research paper

## A Multi-Facet-Effectuator Soft Robot in Polyhedral Configuration for Multidirectional Function Reuse



Yige Wu <sup>a</sup> , Nan Huang <sup>a</sup>, Shaowu Tang <sup>a</sup> , Xiaohuang Liu <sup>a</sup>, Xianxu Li <sup>a</sup> , Sicong Liu <sup>b,c,\*</sup> , Juan Yi <sup>d</sup>, Zheng Wang <sup>e</sup> , Jian S Dai <sup>a,\*</sup>

<sup>a</sup> Department of Mechanical and Energy Engineering, Southern University of Science and Technology, Shenzhen, Guangdong, 518000, China

<sup>b</sup> Sino-German College of Intelligent Manufacturing, Shenzhen Technology University, Shenzhen, Guangdong, 518055, China

<sup>c</sup> Guangdong Provincial Key Laboratory of Intelligent Morphing Mechanisms and Adaptive Robotics, Harbin Institute of Technology (Shenzhen), Shenzhen, Guangdong, 518055, China

<sup>d</sup> School of Advanced Engineering, Great Bay University, Dongguan, Guangdong, 523000, China

<sup>e</sup> Wisson Robotics, Shenzhen, China

## ARTICLE INFO

**Keywords:**  
soft robotics  
Polyhedral robots  
Function reuse  
Robot Design

## ABSTRACT

Soft robots offer flexibility in unstructured environments, though many designs remain tailored to specific tasks. In this paper, we propose an innovative approach employing Multi-Facet-Effectors (MFEs) in polyhedral configuration for the design of a soft robot. In particular, three Soft-Bellowed Actuators (SBAs) constitute the identical triangle effector in each facet of an octahedral-shaped configuration. Utilizing the effector's two distinct motion forms—Uniform Scaling Motion (USM) and Coordinated Deformation Motion (CDM), the MFE robot functions both as gulp grippers (MFG) and parallel arms (MFA), exhibiting versatile capabilities without intricate designs. A topological analysis using the POC equation validates MFE design's 6 degrees-of-freedom (DOFs) movements. The robot exhibits 5 symmetric DOFs and an asymmetric translational DOF along the Z-axis. The rotation around the Z-axis achieving 35.7°. The robot is able to grasp objects within a diameter range of 36.3–109.1 mm, with the maximum holding force up to 7 N. Forward and inverse kinematics models for the MFA movements are established and validated. An RMS error of 1.6 mm in translation and 0.9° in rotation is achieved, with a maximum in-plane error of 3.97 mm. Demonstrations of multi-facet manipulation, climbing, and object retrieval validate the benefits of multidirectional function reuse.

## 1. Introduction

Soft robots have attracted significant attention in recent years [1,2] due to their inherent compliance and deformability. These characteristics enable soft robots to exhibit remarkable adaptability across various applications, such as wearable devices, underwater manipulations, and dexterous grasping [3–6], and diverse locomotion tasks including crawling, climbing, and terrain exploration [7]. Such adaptability fundamentally arises from their ability to safely and effectively interact with uncertain environments. In particular, these interactions often rely on two essential capabilities—manipulation (including grasping) and locomotion—which together allow soft robots to perform a wide range of tasks.

\* Corresponding authors.

E-mail addresses: [liusicong@sztu.edu.cn](mailto:liusicong@sztu.edu.cn) (S. Liu), [daijs@sustech.edu.cn](mailto:daijs@sustech.edu.cn) (J.S. Dai).

Grasping secures objects against external disturbances, while manipulation applies forces that reorient or reposition them relative to the reference frame of the robotic hand [8,9]. Manipulation capabilities can be strengthened by increasing degrees of freedom (DOFs) [10]. Researchers have developed multiple strategies to enhance soft-robot interaction capabilities with the environment [11–15]. For instance, studies have reported flexible-axis-driven soft robotic grippers capable of simultaneously grasping and rotating bottle caps [16], as well as octopus-like soft arms that can reach, grasp, and interact with objects in unstructured environments [17, 18]. By improving the robots' structural design, these approaches provide greater deformability, compliance, and operational flexibility. Despite these advances, existing studies have predominantly concentrated on end-effector manipulation, and comparatively less attention has been given to its integration with whole-body motions.

Alongside manipulation, locomotion constitutes another fundamental capability of soft robots. Researchers have developed diverse locomotion strategies for soft robots, including crawling, rolling, climbing, and shape-reconfigurable movements which enable robots to modify their gaits or body shapes to suit different environments [19,20]. For instance, inspired by spiders and caterpillars, soft robots have been designed to deform and adapt locomotion modes for efficient navigation in complex terrains [21,22]. Pneumatically actuated soft robots, capable of large deformations under pressurization, have been applied in tasks such as climbing cylindrical objects, exemplified by soft pipe-climbing robots [23,24]. In addition, researchers have also applied the Stewart platform mechanism to design a soft robotic arm which obtained flexible six DOFs motions [25,26]. These advances in locomotion reinforce the versatility of soft robots and set the foundation for multifunctional robots that unify manipulation and locomotion.

Building on these insights, modular design has been combined with actuation strategies to enable soft robots with both motion and manipulation capabilities [27–32]. Examples include ant-inspired robots with task-specific limbs [33], and octopus-like robots using different arms for grasping and movement [34]. Yet, current designs still rely on distinct structures to fulfill specific functions, which limits functional flexibility and increases structural complexity. Researchers are exploring strategies that employ repetitive, identical structural modules capable of performing both locomotion and manipulation [35,36]. Among these, polyhedral soft robots have emerged as a promising direction for multifunctionality. For example, the isoperimetric soft robot employs reconfigurable inflatable tube trusses, enabling untethered movement and manipulation [37]. The tetrahedral robot uses extensible pneumatic actuators for shape adaptation, allowing rolling, crawling, and bounding [38]. A stackable design [39] utilizes mesh-based pneumatic muscles to rapidly form 3D structures capable of multi-modal locomotion. These designs face trade-offs between structural and control complexity, motion flexibility, and functional diversity. Most of them primarily emphasize locomotion capabilities, while exhibiting limited manipulation performance. Moreover, limited attention has been paid to achieving tightly integrated motion-manipulation synergy within a unified topological framework.

In contrast, a Multi-Facet-Effector (MFE) soft robot proposed in this work introduces a novel octahedral configuration that uniformly distributes regular polygonal effectors across each facet, enabling functional reuse and simplified control. Unlike prior designs,

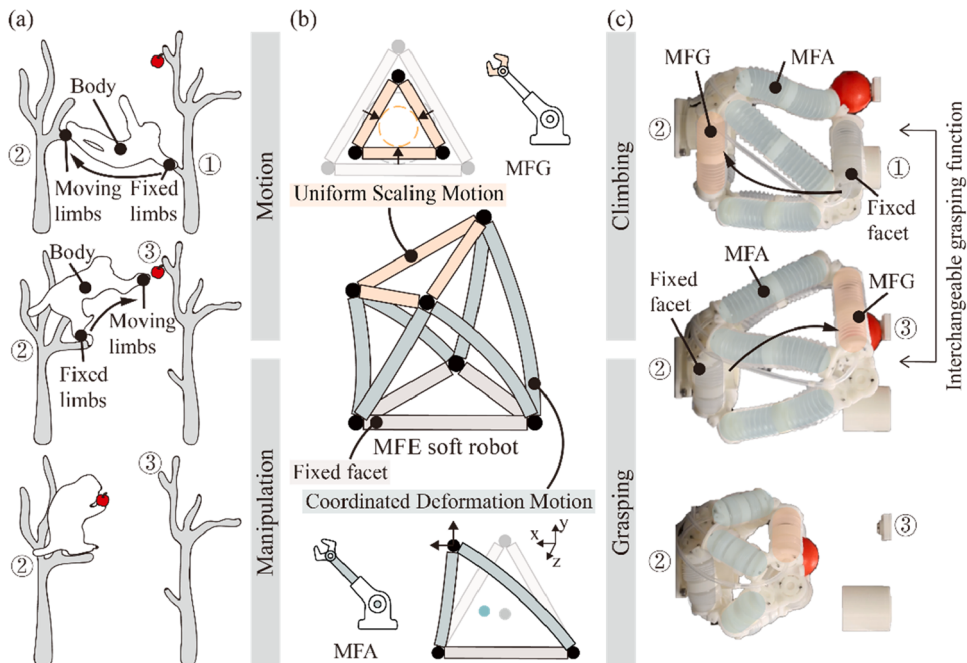


**Fig. 1.** The concept of MFE design. (a) The primates use upper and lower limbs in an alternating fashion to grab and navigate between tree trunks. (b) A facet-effector, composed of three identical soft actuators arranged in a 2D triangular configuration, enables two motion forms: the USM and the CDM—which correspond to two functional modes: the MFG and the MFA. The facet-effectors are assembled into a multi-facet-effectors robot with an octahedra structure. (c) Motion and manipulation of primates inspire the MFE soft robot to accomplish continuous grasping and climbing by the coordinate movements of multi-facet-effectors.

the MFE robot integrates distinct motion forms and supports function switch between manipulation and locomotion. This multi-functionality empowers versatile 6-DOF motions and grasping capabilities at each facet, significantly expanding the robot's operational versatility.

This work makes the following contributions:

- The MFE soft robot utilizes regular polygonal effectors uniformly distributed across each facet of a polyhedron, enabling functional reuse. The effector features two distinct motion forms—Uniform Scaling Motion (USM) and Coordinated Deformation Motion (CDM)—and can switch between a gulp grasping (MFG) mode and a parallel arm (MFA) mode. This enables grasping at each facet as well as versatile 6-DOF motions.
- A topological analysis approach is introduced into the octahedral structure design, utilizing the Position and Orientation Characteristics (POC) equation to analyze and validate the DOFs of the design. Forward and inverse kinematic models are developed and verified, demonstrating the feasibility of the modeling.
- The effectiveness of the proposed modeling and control strategies is experimentally validated, showcasing significant advantages in tasks such as multidirectional operation and climbing in complex 3D environment. The results confirm the robot's practicality and performance.
- Section II of this paper explores the concept, design, and implementation of MFE in a soft robot. Section III introduces the modeling and control of an octahedral MFE structure. Section IV showcases the robot's performance through experiments in two modes. Section V validates the functionality of the robot through experiments. Section VI concludes the work.

## 2. Concept and design

Functional reuse is commonly observed in the evolutionary adaptations of organisms, allowing them to perform diverse locomotive functions across environments. For example, the tentacles of octopuses are not only used for grasping but also for swimming and crawling. This multifunctionality of body structure allows them to be highly adaptable in complex environments. The MFE soft robotic structural design, proposed in this study, is inspired by the interchangeable grasping function of the upper and lower limbs of primates, allowing the arms to hook onto one tree branch while the feet hook onto another when navigating through trees. Alternating between upper and lower limbs, the animal can achieve seamless and consecutive movements through randomly located tree branches as shown in Fig. 1(a). Fig. 1(b) shows a scalable two-dimensional (2D) triangle with the linear soft actuators forming the three sides. The triangle exhibits uniform scaling (USM) and coordinated deformation motion (CDM) forms that can be conceptualized as a facet-effector, which enable it to function as a gulp gripper (MFG) when the actuators elongate and contract uniformly, and as a parallel arm (MFA) when the actuators deform coordinately. By implementing the facet-effectors as the discrete surfaces of a polyhedral, this concept expands to constitute 3D configurations that lead to a MFE robot. Every facet-effector possesses two functional modes. Thus, the MFE robot can function versatilely as grippers and arms. Through the repositioning of grippers and arms, the robot achieves functions like climbing or performing operations in 3D space using the interchangeable functionality of the multi-facet-effectors (Fig. 1(c)).

### 2.1. Facet-effector design

To achieve multi-DOF mobility in a closed-loop form, we use three identical soft-bellowed actuators (SBAs) to form a facet-effector unit with an equilateral triangle design. By controlling the input pressure, the facet-effector can perform the motion forms the USM and the CDM. In USM, all actuators deform uniformly to form a variable-radius gulp gripper (Fig. 2(a)). In CDM, one SBA is fixed while the

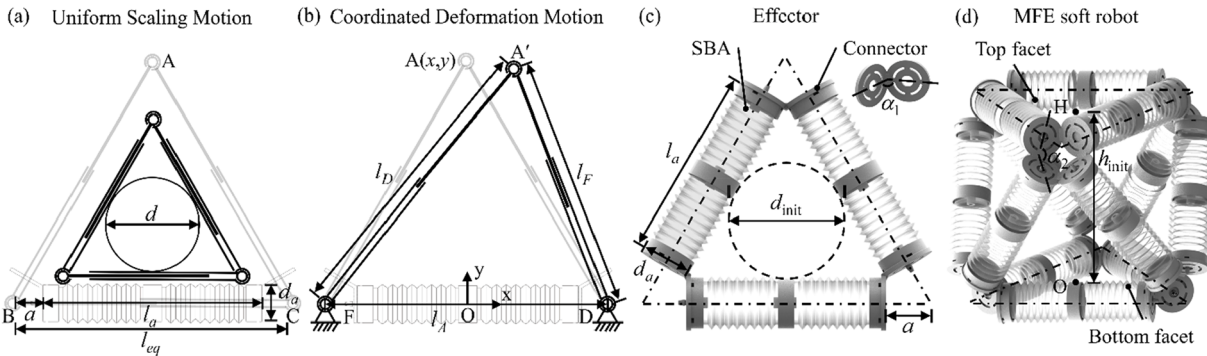


**Fig. 2.** The design overview showcases the components of the MFE soft robot in an octahedral configuration. (a) Uniform Scaling Motion (USM) features a wide-opening grasp mechanism designed for enveloping and securing objects. (b) In Coordinated Deformation Motion (CDM), the actuators coordinate their deformations to position and manipulate objects with synchronized arm movements. (c) The 2D facet-effector consists of three evenly spaced, closed-loop soft-bellowed actuators (SBAs), which provide linear expansion and contraction. (d) The MFE design demonstrates how the facet-effectors are integrated to enable complex, multi-directional movements.

lengths of the other two are varied, enabling the structure to generate 2-DOF movements at the vertex A (Fig. 2(b)).

This design is chosen for its ability to distribute forces uniformly, ensuring stable interactions with the external environment. As shown in Fig. 2(c), the SBA obtains linear expansion and contraction capabilities as well as omnidirectional flexibility. Each SBA comprises two bellows, a bellow connector, and two end caps. The bellows determine the deformability, while the bellow connector enhances structural stiffness. Actuators can be designed based on functional requirements, with parameters such as dihedral angle, thickness, and material being crucial considerations. The bellows are selected based on validated design parameters from previous studies [40–42], ensuring sufficient motion range and flexibility for the effector's operation. Table 1 lists the parameters of the SBA used in this design. The bellows are low-cost and mass-produced using molded plastic, and the other components are produced by stereolithography (SLA) 3D printing with photopolymer resin. Post-processing involves adding a silicone layer to the bellow connector to enhance contact friction and bonding components with hot melt adhesive. A cylindrical protrusion slightly smaller than the bellows opening diameter is designed on the end cap. When the hot-melt adhesive is applied and the bellows is pressed onto the end cap, the glue flows into the inner wall of the bellows interface. The adhesive forms interlocking seal structure after solidification, which provides reliable airtight performance. It is important to ensure sufficient preheating and to perform the bonding process promptly. The end caps are designed to connect directly to the air tube, and it has preset holes for simple assembly and maintenance using screws and nuts. The facet-effector's modular and easily assembled architecture enables rapid creation of three-dimensional configurations with triangular facets.

## 2.2. MFE soft robot

Following the bio-inspired limb-alternating behaviors, a modular configuration approach is adopted to construct a robotic system capable of multiple motion modalities. Unlike the state-of-the-art tetrahedron-configuration robots [26,43,44], we choose the configuration of a regular octahedron for the design of the robot, which offers adequate flexibility without introducing excessive complexity [45–47]. This design endows the robot with eight facet-effectors and twelve SBAs (Fig. 2(d)). The configuration possesses multiple identical facets with interchangeable functions, i.e. a facet-effector can function as a gripper while other effectors can act as arms simultaneously, thus achieving a combination of mobility and manipulation.

## 2.3. Validation of design

To validate the design, a topological analysis approach, namely, the POC equation is adopted [48–50] to describe the motion characteristics and behavior of the moving facets relative to a fixed base, as shown in Fig. 3. The POC set-based method employs six elements to describe the relative motion characteristics between two links. Among these, three elements represent the position and orientation characteristics of relative rotation, while the other three describe those of relative translation. This method is independent from the specific configuration of the mechanism and does not rely on the existence of a fixed coordinate system. Based on velocity analysis of kinematic pairs, the POC set representations for prismatic pairs (P pairs) and revolute pairs (R pairs) can be derived.

Here, the POC set of a P pair is defined as  $M_P = [t^1(\parallel P), r^0]$ , where  $r^0$  represents no finite rotation,  $t^1(\parallel P)$  represents a finite translation along direction of the P pair. The POC set of an R pair is defined as  $M_R = [t^1(\perp R, \rho), r^1(\parallel R)]$ , where  $r^1(\parallel R)$  represents a finite rotation parallel to axis of the R pair,  $t^1(\perp R, \rho)$  represents a finite translation for the base point o' along the direction perpendicular to the plane formed by axis of the R pair and the radius vector  $\rho$ .

Since the motion of a parallel mechanism depends on the coordinated behavior of its limbs, the POC equation employs an intersection operation to compute the resultant motion characteristics as  $M_{Pa} = \cap_{j=1}^m M_{bj}$ , where  $M_{Pa}$  denotes the POC set of the moving platform,  $M_{bj}$  represents the POC set of the end link of the j-th limb,  $m$  is the total number of limbs in the parallel mechanism.

When the facet-effector is considered as the lateral triangle of a parallel mechanism, one edge of the triangle is fixed as the base. This configuration can be simplified to the 2-DOF mechanism shown in Fig. 3(a). The simplification is based on the axial extensibility and omnidirectional flexibility of the bellows and structural constraints. In the planar case, the rod connecting the end-effector and the midpoint of the fixed edge can rotate around the fixed point and extend along its axis, which corresponds to one revolute and one prismatic joint. Therefore, the corresponding POC equation is given as follows,

$$\mathbf{M}_s = \begin{bmatrix} t^1(\perp R_1) \\ r^1 \end{bmatrix} \quad (1)$$

where  $t^1(\perp R)$  signifies one translation in a direction within a plane perpendicular to axis of R pair,  $r^1$  indicates one rotation.

**Table 1**  
Geometric Parameters of the Design.

$d_a$	Diameter of the actuator	36.3mm
$l_a$	Static length of the actuator	133.0mm
$a$	Distance between the center of two caps	32.6mm
$\alpha_1$	Angle between the left and right caps	120°
$\alpha_2$	Angle between the up and down caps	120°
$d_{init}$	Static inner diameter of the effector	78.1mm
$h_{init}$	Static distance between parallel faces	161.8mm

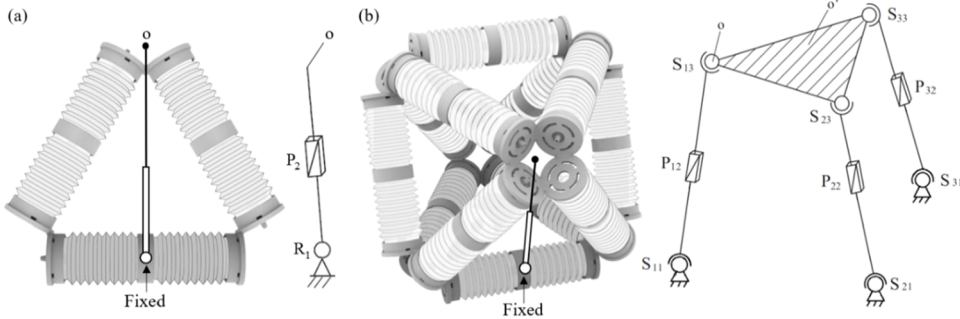


**Fig. 3.** The POC equation is applied for topological validation of the regular octahedral design. (a)  $\{-R(\perp P)-\}$  topology, a single planar triangular unit is simplified by fixing one edge as a revolute joint, with the upper moving vertex denoted as point  $o$ . (b)  $3-SOC\{-S-P-S-\}$  PM topology, the octahedral configuration of the polyhedral soft robot is further simplified as a parallel mechanism consisting of three connecting links, with both the upper and lower connections modeled as spherical joints.

For the MFE structure, one facet is selected as the base for analysis. Within the plane formed by the equivalent rod and the fixed edge, the rod exhibits the same two degrees of freedom as in Fig. 3(a). In the spatial configuration (Fig. 3(b)), this plane can rotate in three-dimensional space about the fixed edge, introducing an extra rotational degree of freedom. Therefore, the structure can be equivalently modeled as a combination of a spherical joint and a prismatic joint. This configuration can be simplified to the 6-DOF mechanism. The POC equation for the parallel mechanism is established based on the intersection calculation rule,

$$\begin{aligned} \mathbf{M}_{pa} &= \left[ \begin{array}{c} t^3 \\ r^3(o_{13}) \end{array} \right] \cap \left[ \begin{array}{c} t^3 \\ r^3(o_{23}) \end{array} \right] \cap \left[ \begin{array}{c} t^3 \\ r^3(o_{33}) \end{array} \right] \\ &= \left[ \begin{array}{c} t^3 \cap t^3 \cap t^3 \\ r^3(o_{13}) \cap r^3(o_{23}) \cap r^3(o_{33}) \end{array} \right] \\ &= \left[ \begin{array}{c} t^3 \\ r^3 \end{array} \right] \end{aligned} \quad (2)$$

where  $t^3$  denotes three translational DOFs,  $r^3$  denotes three rotational DOFs,  $o_{ij}$  represents the location of the  $j$ -th kinematic pair on the  $i$ -th limb, corresponding to the position of the ball joint that enables spatial rotation.

The POC analysis enables topological-level evaluation of the mechanism's degrees of freedom, independent of specific geometric parameters. Building upon this topological understanding, the regular octahedron design demonstrates distinct advantages: 1) The DOF are not reduced due to excessive coupling. In the design, when a single unit is considered as a triangle with the base fixed, its DOF is 2 according to Eqn. (1). By combining three such units to form a parallel topological structure, the overall DOF achieves 6 as indicated by Eqn. (2), ensuring the flexibility and mobility of the structure without a reduction in DOF caused by over-coupling. 2) Each facet can serve as a grasping surface for operation.

This reusability is enabled not only by the mechanical configuration but also by the high topological symmetry of the octahedron, which allows all triangular facets to serve interchangeably as grippers or actuators. The structural equivalence simplifies directional control and enables the reuse of identical actuation patterns across facets, reducing control complexity and supporting task transitions with minimal reorientation.

### 3. Modeling and control

#### 3.1. Facet-effector modeling

The SBA exhibits the required active actuation and compliance, achieving bidirectional linear motion through contraction and elongation by varying the pressure. In the static model of SBA, changes in pressure  $\Delta P$  primarily cause linear displacement  $\Delta l$  and longitudinal force  $F_l$ . Consequently, the actuator's behavior can be presented as follows

$$\Delta l = \frac{\Delta P S - F_l}{k_l} \quad (3)$$

By arranging multiple SBAs within a 2D closed polygon, the effector converts the linear motion of the bellows into radial motion and provides 2-DOF mobility at the vertex. This configuration enables the USM and the CDM motion forms.

During USM, the actuators elongate and contract together, allowing the effector to grasp objects by wrapping around them. The kinematic model captures the relationship between the actuator input pressure and the gripping diameter. The three sides of the effector are equal, denoted as  $l_{eq}$ , and the gripping diameter (i.e., the diameter of the inscribed circle) is denoted as  $d$ , as shown in Fig. 2(d). Using geometric relationships, we can obtain

$$d = \frac{\sqrt{3}}{3}l_{eq} - d_a = \frac{\sqrt{3}}{3}(l_a + 2a) - d_a \quad (4)$$

where  $l_a$  corresponds with input pressure.

During CDM, the actuators' deformations are coordinated to achieve positioning. The kinematic model maps the actuator inputs to the end-effector's movement (Fig. 2(e)). Assume the three vertices of the effector are A, F, and D, with the triangle's sides denoted as  $l_A$ ,  $l_F$  and  $l_D$ , where  $l_A$  is the fixed side length. The two SBAs  $l_F$  and  $l_D$  can extend and contract within a certain length range. Let the coordinates of the end movable point A be  $(x, y)$ , with the origin at the midpoint of  $l_A$  and the X-axis aligned with  $l_A$ . Given the relationship between the input pressures  $p_D$  and  $p_F$  corresponding to  $l_D$  and  $l_F$ , respectively, the coordinates of point A can be determined:

$$x = \sqrt{l_D^2 - \frac{(l_F + l_D + l_A)(-l_F + l_D + l_A)(l_F - l_D + l_A)(l_F + l_D - l_A)}{l_A^2}} - \frac{l_A}{2}, \quad (5)$$

$$y = \frac{\sqrt{(l_F + l_D + l_A)(-l_F + l_D + l_A)(l_F - l_D + l_A)(l_F + l_D - l_A)}}{l_A}.$$

### 3.2. Forward kinematics of octahedral MFE structure

In the kinematic modeling of the MFE, the connectors are considered as rigid elements, while the SBAs are modeled as telescopic actuators with spherical joints at both ends. The centers of the ball joints coincide with the centers of the SBA end faces, and the axis of

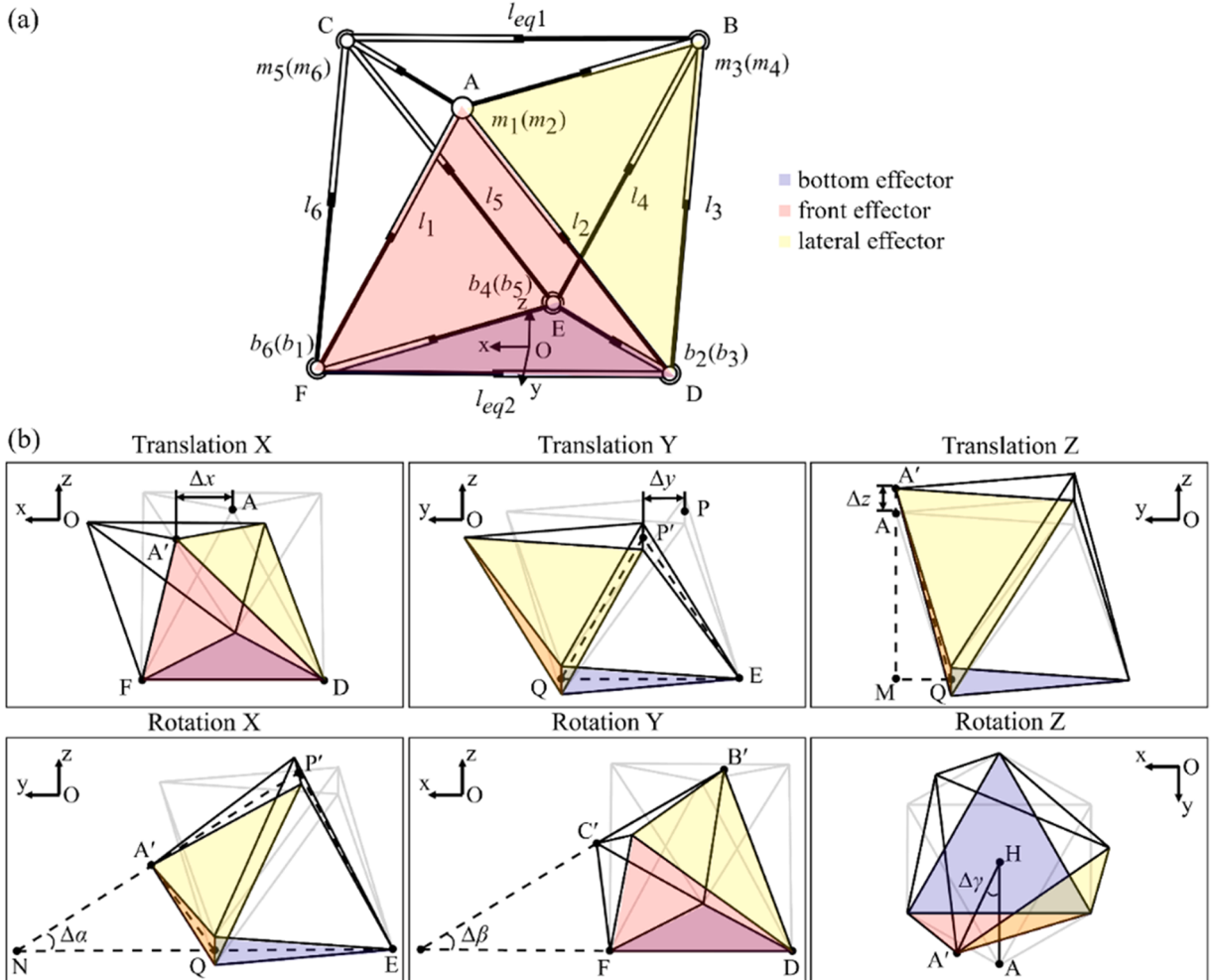


**Fig. 4.** The kinematic model of the MFE soft robot. (a) Comprehensive mechanism diagram applicable to both forward and inverse kinematics, providing a unified representation of the system's structure and movement. (b) Geometric diagram illustrating the six degrees of freedom (DOFs) in forward kinematics, where the top and bottom facets are fixed, and the SBAs within the body are capable of deformation.

the slider is collinear with the axis of the SBA. Based on this, a schematic diagram of the mechanism can be established, as shown in Fig. 4(a).

The forward kinematics model is built to obtain the relationship between the length of SBAs and the movement of the top facet. In the model, all the lengths  $l = l_a + 2a$ . It is assumed that the SBAs of the upper and lower effectors denoted as  $l_{eq1}$  and  $l_{eq2}$ , respectively, are equal in length and fixed. The original lengths of  $l_{eq1}$ ,  $l_{eq2}$  and  $l_1 - l_6$  are designated as  $l_0$ . Defining the direction parallel to  $DF$  as the X-axis, perpendicular to  $DF$  as the Y-axis, and vertically upward as the Z-axis, originating from point  $O$ . The geometry diagrams of six DOFs are illustrated in Fig. 4(b). The known condition of the input pressures corresponds to the lengths  $l_1 - l_6$ . The resulting movements are categorized into translations, denoted as  $\Delta x$ ,  $\Delta y$ ,  $\Delta z$ , and rotations, denoted as  $\theta_x$ ,  $\theta_y$ ,  $\varphi_z$ . The transformations of the system are described using two matrices:  $t$  for translation and  $r$  for rotation.

For translational motion,  $\Delta x$ ,  $\Delta y$  and  $\Delta z$  are determined by the displacements of the top surface's center point  $H$ , which transforms into  $H'$  after movement. Using Heron's formula, the coordinates of the top surface points can be calculated based on the known edge lengths, and the translation vector  $\overrightarrow{HH'}$  is subsequently derived. The matrix  $t$  can be obtained as

$$\mathbf{t} = \begin{bmatrix} \Delta x \\ \Delta y \\ \Delta z \end{bmatrix} = \begin{bmatrix} x_{H'} - x_H \\ y_{H'} - y_H \\ z_{H'} - z_H \end{bmatrix} \quad (6)$$

For rotational motion,  $\theta_x$  and  $\theta_y$  represent the angles between the top surface and the X- and Y-axis, while  $\varphi_z$  is the rotation angle of the top surface about the Z-axis. Assumed that the curvature remains constant. Under this assumption, the relationships  $PN = EN$  and  $A'N = QN$  are established, enabling the calculation of the coordinates of three points on the top surface. The normal vector of the plane  $\vec{n} = (n_x, n_y, n_z)$  can be obtained from the coordinates of the three points, which allows the angles between the plane and the X- and Y-axis to be calculated. For rotation about the Z-axis, the equation can be formulated because the radius of the circumcircle of  $\triangle ABC$  remains unchanged, which allows  $\varphi_z$  to be determined. The matrix  $r$  can be obtained as

$$\mathbf{r} = \begin{bmatrix} \theta_x \\ \theta_y \\ \varphi_z \end{bmatrix} = \begin{bmatrix} \cos^{-1}\left(\frac{|n_x|}{\sqrt{n_x^2 + n_y^2 + n_z^2}}\right) \\ \cos^{-1}\left(\frac{|n_y|}{\sqrt{n_x^2 + n_y^2 + n_z^2}}\right) \\ \varphi_z \end{bmatrix} \quad (7)$$

Assuming  $A (a_x, a_y, a_z)$  becomes point  $A' (a'_x, a'_y, a'_z)$  after translating along the X-axis, and focusing on  $\triangle AFD$  and,  $\triangle A'FD$ , Translation X can be obtained as

$$\Delta x = a'_x - a_x = \frac{l_1^2 - l_2^2}{2l_0} \quad (8)$$

Translation Y can be obtained similarly as

$$\Delta y = p'_y - p_y = \frac{l_3^2 - l_4^2}{\sqrt{3}l_0} \quad (9)$$

Assuming  $M$  is the perpendicular projection of  $A'$  onto the base, and focusing on  $\triangle AMQ$  and  $\triangle A'MQ$ , the length of  $MQ$  remains unchanged, i.e.

$$a_z = \frac{\sqrt{6}}{3}l_0, a'_z = \sqrt{A'Q^2 - MQ^2}, \quad (10)$$

where  $MQ = \sqrt{AQ^2 - AM^2} = \frac{\sqrt{3}}{6}l_0$  and  $A'Q = \sqrt{l_1^2 - \left(\frac{l_0}{2}\right)^2}$ . Translation Z is simplified into,

$$\Delta z = a'_z - a_z = \sqrt{l_1^2 - \frac{1}{3}l_0^2} - \frac{\sqrt{6}}{3}l_0. \quad (11)$$

Assuming and the curvature is constant,  $P'N = EN$  and  $A'N = QN$ , Rotation X can be obtained as

$$\Delta \alpha = \frac{P'E - A'Q}{\frac{\sqrt{3}}{2}l_0} = \frac{\sqrt{l_1^2 - \left(\frac{l_0}{2}\right)^2} - \sqrt{l_4^2 - \left(\frac{l_0}{2}\right)^2}}{\frac{\sqrt{3}}{2}l_0}. \quad (12)$$

Rotation Y can be obtained similarly as

$$\Delta\beta = \frac{B'D - CF}{\frac{\sqrt{3}l_0}{2}} = \frac{l_3 - l_6}{\frac{\sqrt{3}l_0}{2}}. \quad (13)$$

Assuming  $h$  is the distance between parallel faces, and  $r_0$  is the circumradius of  $\Delta ABC$  which remains unchanged,

$$\begin{cases} {a'_x}^2 + {a'_y}^2 = r_0^2 \\ {(a'_x - f_x)}^2 + {(a'_y - f_y)}^2 + h^2 = l_1^2 \\ {(a'_x - d_x)}^2 + {(a'_y - d_y)}^2 + h^2 = l_2^2 \end{cases} \quad (14)$$

where  $r = \frac{l_0}{\sqrt{3}}$ ,  $d_x - f_x = l_0$ ,  $d_y - f_y = 0$ , Rotation Z is simplified into

$$\Delta\gamma = \arccos \sqrt{1 - \left( \frac{\sqrt{3}(l_1^2 - l_2^2)}{2l_0^2} \right)^2} \quad (15)$$

### 3.3. Inverse kinematics of octahedral MFE structure

For the inverse kinematics model, the vectors representing the contact points between SBAs  $l_1 - l_6$ , the rigid connectors on the moving platform are denoted as  $m_1 - m_6$ , and the vectors representing the contact points on the bottom platform are denoted as  $b_1 -$

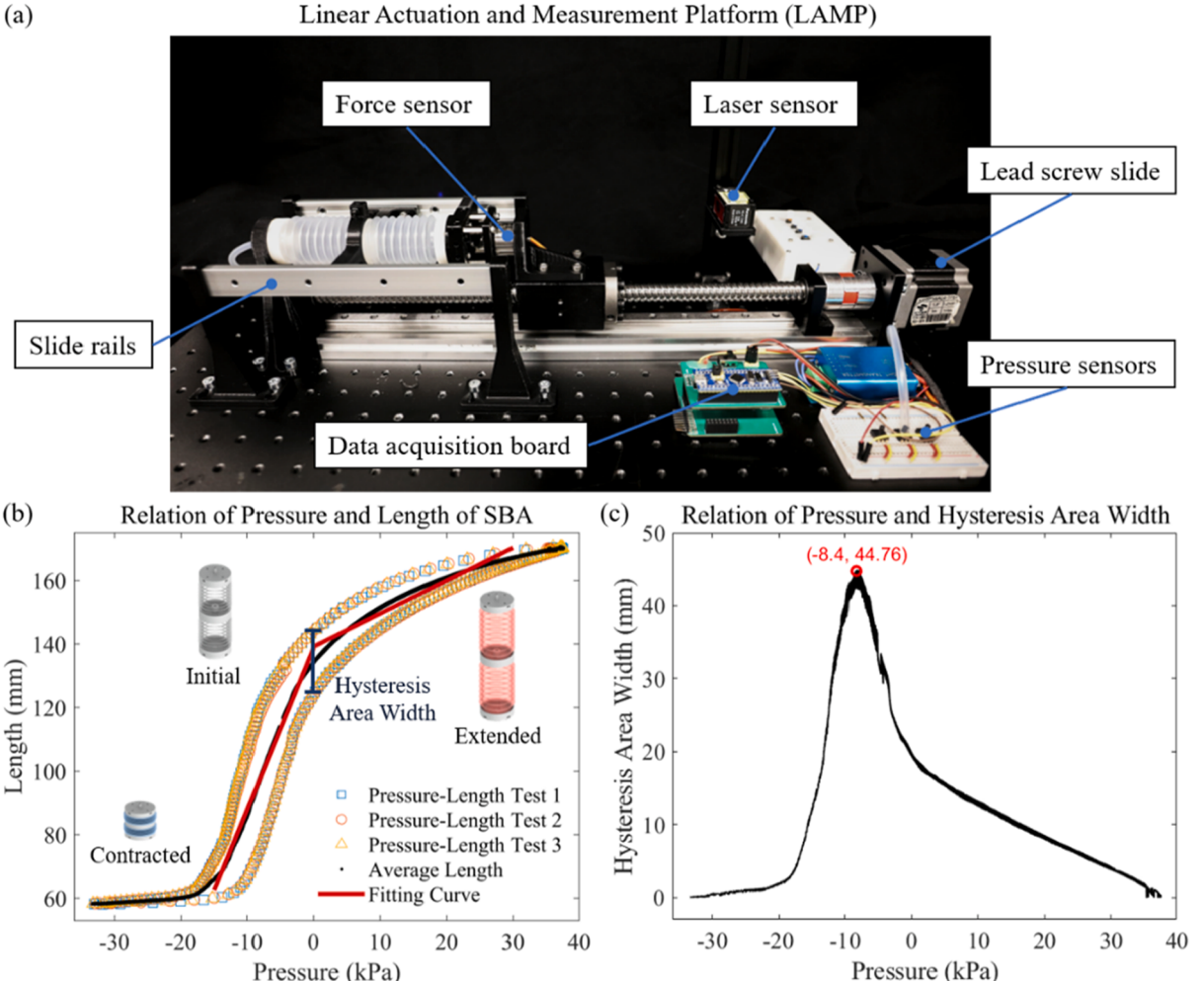


**Fig. 5.** Performance testing of the SBA. (a) The experimental setup, which includes the lead screw stage, pressure sensor, laser sensor, and force sensor. (b) Test results of SBA's length variation under different pressure conditions without external force applied. (c) Pressure-dependent hysteresis width, indicating peak viscoelastic effects near  $-8.4$  kPa and reduced hysteresis at higher pressures.

$b_6$ , as shown in Fig. 4(a). The vectors defined as follows

$$\begin{aligned} m_1(m_2) &= \overrightarrow{OA}, m_3(m_4) = \overrightarrow{OB}, m_5(m_6) = \overrightarrow{OC}, \\ b_2(b_3) &= \overrightarrow{OD}, b_4(b_5) = \overrightarrow{OE}, b_6(b_1) = \overrightarrow{OF}. \end{aligned} \quad (16)$$

These vectors satisfy the following relationships,

$$\begin{aligned} |m_1 - m_3| &= |m_3 - m_5| = |m_5 - m_1|, \\ |b_2 - b_4| &= |b_4 - b_6| = |b_6 - b_2|. \end{aligned} \quad (17)$$

Therefore, the inverse kinematics model is presented as

$$l_i = m_i - b_i = Tsm'_i - b_i \quad (18)$$

where  $l_i$  denotes the length of the  $i$ -th SBA,  $m_i$  denotes the homogeneous coordinates of the centers of the SBA end faces on the upper facet,  $b_i$  denotes the centers on the base facet in the base platform frame, and  $m'_i$  is the coordinates in the moving platform frame, as shown in Fig. 4(a).  $s$  represents the scaling factor of the top and bottom surfaces, which can be scaled to simulate the function of a gripper. According to the Denavit–Hartenberg matrix method,  $T$  is the transformation matrix which includes rotations and translations,

$$T = \begin{bmatrix} R & p \\ 0 & 1 \end{bmatrix} \quad (19)$$

The rotation matrix  $R$  is calculated by the rotations  $R_Z(\gamma)$ ,  $R_Y(\beta)$  and  $R_X(\alpha)$ . The position vector  $p$  is given as follows,

$$R = \begin{bmatrix} \cos\gamma\cos\beta & \cos\gamma\sin\beta\sin\alpha - \sin\gamma\cos\alpha & \cos\gamma\sin\beta\cos\alpha - \sin\gamma\sin\alpha \\ \sin\gamma\cos\beta & \sin\gamma\sin\beta\sin\alpha + \cos\gamma\cos\alpha & \sin\gamma\sin\beta\cos\alpha - \cos\gamma\sin\alpha \\ -\sin\beta & \cos\beta\sin\alpha & \cos\beta\cos\alpha \end{bmatrix}, p = \begin{bmatrix} \Delta x \\ \Delta y \\ \Delta z + h \end{bmatrix}, \quad (20)$$

where  $\Delta x$ ,  $\Delta y$ , and  $\Delta z$  are the translation displacements in X, Y, and Z-axis in the universal frame,  $\alpha$ ,  $\beta$ , and  $\gamma$  are the rotation angles around X, Y, and Z-axis in the local frame, respectively.

#### 4. Experimental validation

##### 4.1. Actuator characterization

Experiments are carried out to explore the mechanical characteristics of the actuator and the performance of the robot. The linear actuation and measurement platform shown in Fig. 5(a) is designed to measure the displacement of SBA and output force under pneumatic input. Slow pressure input induces SBA movement along the slide rail, and pressure sensor (XGPZP6857A, CFSensor Inc.) and laser sensor (HG-C1200, Panasonic Inc.) data are recorded. Due to hysteresis effects, deviations are observed between the extension and contraction curves as shown in Fig. 5(b). To further characterize this behavior, the pressure-dependent hysteresis area width is quantified. As shown in Fig. 5(c), it peaks around  $-8.4$  kPa and decreases as the pressure increases. This trend indicates that the viscoelastic and frictional hysteresis effects are most pronounced in the early stage of pressurization, where material damping and internal resistance dominate. At higher pressures, the deformation becomes more stable and repeatable, suggesting reduced hysteresis and improved actuation consistency.

The actuator undergoes repeat experiments. The averaged data within the practical working range is fitted by segmented linear functions with  $R^2=0.996$ , which is reliable and can simplify subsequent calculations for the model. The segmented fitting is adopted

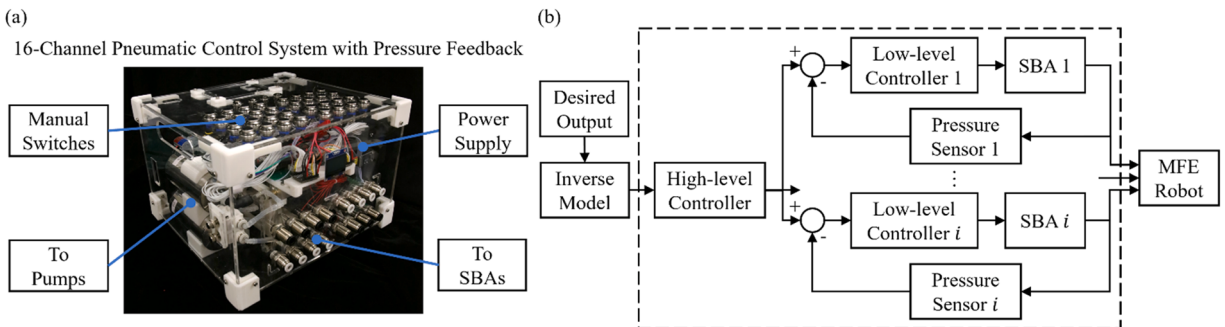


**Fig. 6.** The control system. (a) The hardware system is designed to provide a stable pressure supply for 16 pneumatic channels and to read sensor data. It supports multiple control modes, such as a manual pressure hold mode and an automatic program mode. (b) The control system logic illustrates the operational flow of the system. The inverse kinematics model calculates the required pneumatic inputs. The low-level controller manages pressure holding for each channel and the high-level controller coordinates pressure among channels and makes motion decisions.

because the SBA exhibits different stiffness characteristics during different deformation stages, leading to a change in the slope of the force-displacement curve. The relation is expressed by the following equations,

$$\begin{cases} l = 5.0844p + 138.7415, p < 0 \\ l = 1.0355p + 139.1741, p \geq 0 \end{cases} \quad (21)$$

#### 4.2. Effector characterization

To evaluate the performance of the facet-effector, experiments are carried out to test the relationship between driving pressure and the effector's state under two different functional modes. A 16-channel pneumatic control system with pressure feedback, as shown in

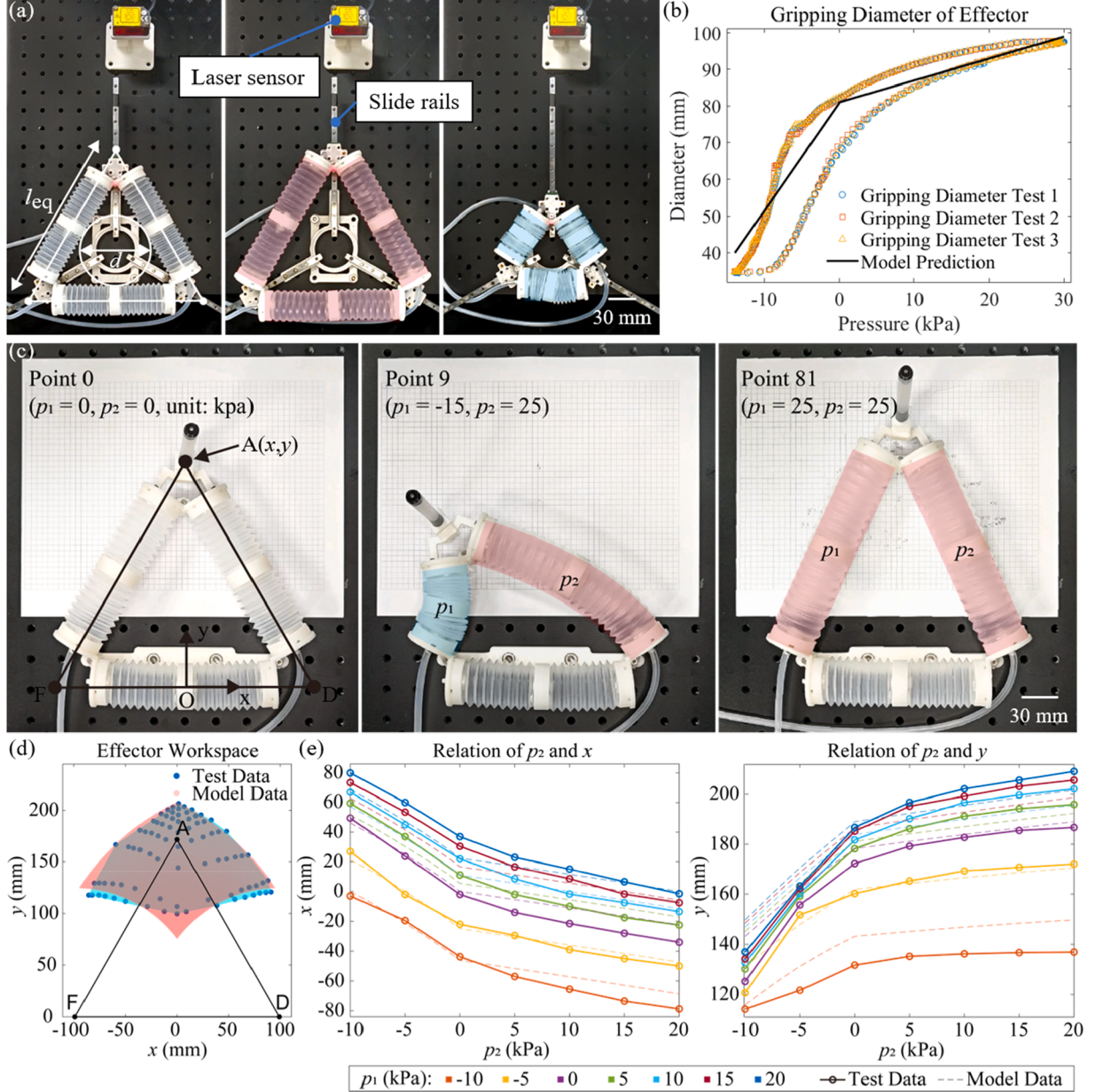


**Fig. 7.** The relationship between input pressure and the effector's performance. (a) Three SBAs are arranged on the diameter test platform, where internal pressure and gripping diameter are measured. (b) The model relationship between pressure and diameter, shown by the black line, aligns with the experimental data. (c) The kinematic model of the effector, illustrating the mapping between actuator inputs and end-effector movement. (d) Comparison of the operational range of the end effector as predicted by the model and as observed in experiments. (e) Experimental and model data illustrating the relationship between applied pressure and end-point positions.

**Fig. 6(a)**, is constructed to facilitate experiments involving pneumatic input and data acquisition. The setup contains a booster pump (KZP-PF, kamoer Inc.) and a vacuum pump (KVP300-KB, kamoer Inc.) to provide the pneumatic supply. The microcontroller (STM32F103C8T6, ST Microelectronics Inc.) regulates the 16 pneumatic channels by controlling optocoupler isolation boards (CA08A, Macrowis Inc.), which in turn controls the solenoid valves (M-DC24V, OST PNEUMATIC Inc.). Each channel is equipped with a pressure sensor (XGZP6857A, CFSensor Inc.). The system also captures data from external sensors: laser sensors (HG-C1200, Panasonic Inc.) for multi-axis displacements, a one-dimensional force sensor (DYMH-103, DAYSENSOR Inc.), a torque sensor (DYJN-104, DAYSENSOR Inc.), and an IMU (JY61, WitMotion Inc.) for angular measurements. Data is collected through the ADC module and serial port and subsequently processed using MATLAB (R2020b, MathWorks). In the experiments, pressurized SBAs are labeled in red, and depressurized SBAs are labeled in blue, and non-pressurized SBAs are marked as blank, controlled by the integrated experimental setup. Control system logic is shown in **Fig. 6(b)**.

In the MFG mode as shown in **Fig. 7(a)**, the diameter test platform is built, consisting of three separate slide rails arranged at 120° intervals and a laser sensor positioned along the diameter direction. Three SBAs are arranged on the platform and connected by pneumatic tubes, which enables them to elongate and contract simultaneously under uniform internal pressure, as shown in **Fig. 7(a)**. The experimental data as shown in **Fig. 7(b)** indicates that the grasping range is approximately 34.9 - 98.7 mm. This range is determined by subtracting the deformed value from the initial distance and converting the diameter from the circumscribed circle to the inscribed circle. Consistent with the single-actuator characterization, the model is established based on the averaged data from both the inflation and deflation phases, thereby reducing the influence of the hysteresis effect. The segmented linear relations obtained from individual actuator experiments are then employed to construct the pressure-diameter relationship. By substituting Eqn. (21) into (4), the model relationship between pressure and diameter is obtained, as illustrated by the black line, which matches the trend of the experimental data.

In the MFA mode as shown in **Fig. 7(c)**, with the ends of one SBA fixed and varying the pressures in the other two SBAs, the moving range of vertex A is tested. A connector is designed to hold a pen at the vertex, allowing for the recording of vertex coordinates through markings. The pressures are recorded by pressure sensors. To illustrate, we plotted 81 points, each corresponding to specific pairs of pressures  $p_1$  and  $p_2$ . The points are organized as follows: For  $p_1$  values of -15 to 25 in increments of 5, each value of  $p_1$  is paired with  $p_2$  ranging from -15 to 25 in increments of 5. This results in 9 points for each  $p_1$ , covering points 1 through 81 in total. **Fig. 7(c)** shows the 0th, 9th, and 81st points from the experimental process. A series of experiments demonstrates the operational range of the end effector under varying pressure conditions, which is then compared to the range predicted by the theoretical model (**Fig. 7(d)**). Due to the

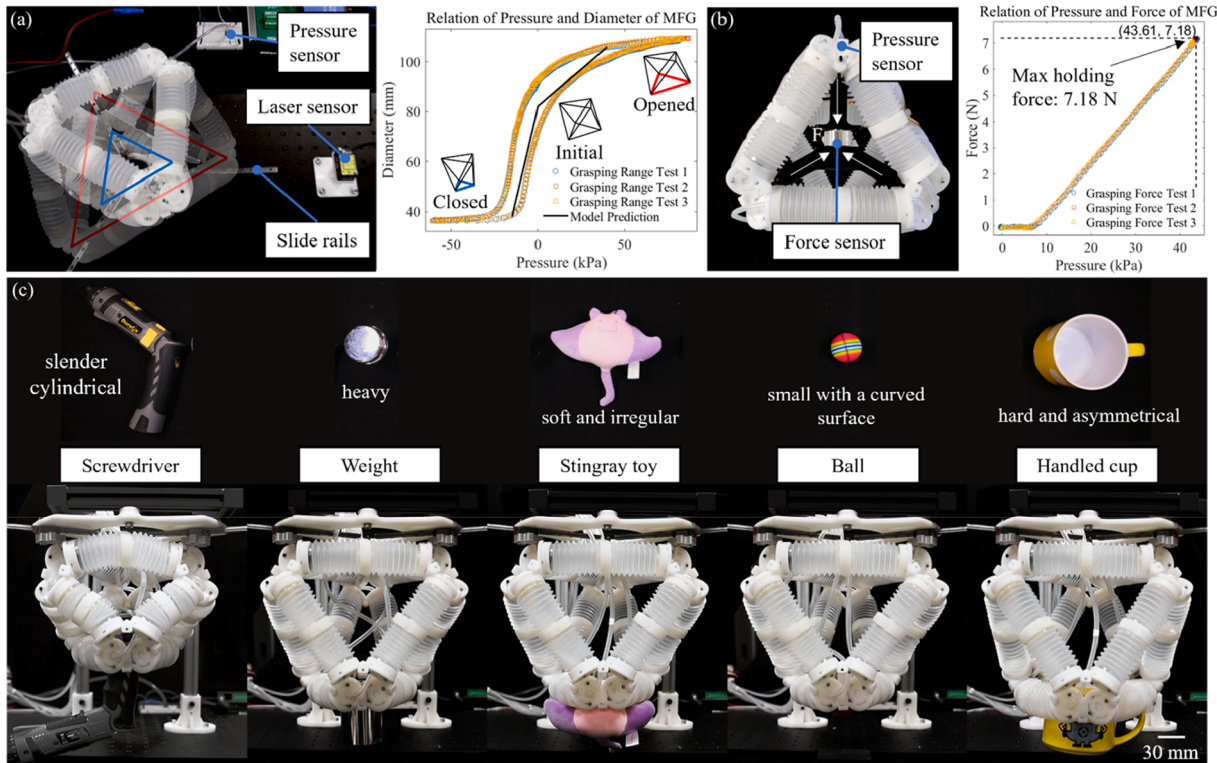


**Fig. 8.** Performance of MFG. (a) The grasping range of MFG, demonstrates its adaptability to objects of various sizes. (b) The grasping force of the MFG is regulated to remain within a safe range, ensuring the maximum force does not exceed limits that could lead to mechanical failure, such as bellow delamination. (c) The MFG's adaptability to grasping objects of diverse shapes, sizes, hardness, and weights is evaluated, highlighting its versatility.

effects of material hysteresis and the order of experiments, there is a slight asymmetry between the left and right sides, while the experimental and model ranges still overlap significantly. Additionally, the relationship between applied pressure and the resulting end positions is examined (Fig. 7(e)), showing that when the pressure of one SBA is fixed, variations in the pressure of the other SBA uniquely affect the coordinates.

#### 4.3. MFG performance

The facet-effector's grasping range, gripping capability, and holding force are evaluated when the robot function as the gulp gripper. As the pressure is regulated, the gripper switches between open and closed states. The gripping diameter is measured by the diameter test platform, ranged from 36.3 to 109.1 mm as shown in Fig. 8(a), which is consistent with the single facet-effector's performance. However, the required pressure to derive the effector significantly increased, Due to the resistance brought from the structural interaction.

In the gripping force test, a force sensor is positioned on the central platform as shown in Fig. 8(b). The maximum pressure applied is 40 kPa, chosen to prevent actuator collapse and ensure stable deformation during grasping force tests. The gripper's deadweight is approximately 111.3 g (without tubes) and is considered negligible in the grasping force measurement, as the sensor records only the contact force with the object in the vertical setup. The force generated by the contraction of the MFG is applied through the contact point of the connector, consistently directed toward the center of the circle. The maximum measured gripping force is approximately 7.2 N, confirming the gripper's holding capability under static conditions. The force-to-weight ratio is compared with that of other pneumatic grippers in the literature that report both gripping force and self-weight. As summarized in Table 2, the MFG achieves a force-to-weight of 6.57, which lies within a moderate range. This parameter is influenced by multiple factors, including material density, applied pressure, and contact conditions.

To further evaluate the gripper's adaptability, five common laboratory objects with varying shapes, sizes, hardness, and weights are selected as shown in Fig. 8(c). The electric screwdriver, characterized by its slender cylindrical handle, is successfully grasped and lifted from the table. The 1kg weight is used to assess the gripper's load-bearing capacity when handling heavy objects. The irregularly shaped stingray toy tests the gripper's ability to handle the soft deformable object with the complex shape. The small ball, with a diameter of 37 mm consists of a smooth curved surface, demonstrates the gripper's effectiveness near its minimum grasping range. Finally, the cup with a handle simulates an asymmetric grasping scenario. The recorded images show that the gripper successfully grasps all five objects, validating the gripper's grasping adaptability.

#### 4.4. MFA performance

The actuation schemes and movements of 6 DOFs with the bottom effector fixed are depicted in Fig. 9, where the circles depict a top-down view of the system. Within each circle, six rectangles are uniformly arranged, representing the six SBAs connecting the top and bottom effectors, numbered as shown. Blank rectangles indicate SBAs without pressure input, red indicate positive, and blue indicate negative pressure input. For Rotation Y and Rotation X, the movements are not limited to pure rotational motion but also involve an associated in-plane displacement, which corresponds to the bending deformation observed during actuation.

The effector's movements and payload are tested in the MFA mode using the kinematic evaluation platform as shown in Fig. 10(a). The angles are recorded by the IMU, displacements are measured by laser sensors, and the pressure inputs are captured by pressure sensors. According to the experimental data, the MFA achieves a translational displacement of approximately 42.2 mm and 54.8 mm in the X and Y directions, respectively, while it extends 29.4 mm and contracts 67.1 mm in the Z direction. Additionally, it can reach rotational displacements of 27.2°, 30.7°, and 35.7° around the X, Y, and Z-axis, respectively. The recorded ranges for these movements are presented in Table 3, limited by the maximum extension and contraction of the SBAs. Apart from the Z-axis translation, five DOFs exhibit symmetric movements in opposite directions.

To validate the forward kinematic model, symmetric inputs of pressurization ranging from 0 to 7.5 kPa and depressurization ranging from 0 to -7.5 kPa are applied. The pressurized SBAs and depressurized SBAs are divided into two groups for actuation, with the grouping and driving methods following actuation schemes. The model and experimental results for the pressure-displacement relationship in the X and Y directions, the pressure-displacement relationship during the extension and contraction process in the Z direction, and the pressure-angle relationship in the three rotational directions are plotted in Fig. 10(b)-(d), respectively. For Z-axis translation, all the actuators are connected, and the abscissa represents the unified pressure. In other cases, the abscissa reflects the pressure difference between the two actuator groups. These plots illustrate the relationship between input pressure and output motion in each DOF. Three sets of data from repeated experiments are displayed.

While the curves display similar trends to the experimental results, the model data exceeds the measured data in most cases, with the exception of the translation along the positive direction of Z-axis. This could be attributed to the coupling observed in the motions

**Table 2**  
Gripping Force Comparison.

Gripper	Peak gripping force (N)	Weight (g)	force-to-weight ratio
SR finger [51]	4.7	750	0.6
MFG	7.2	111.3	6.6
RB50 [52]	20	105	19.4

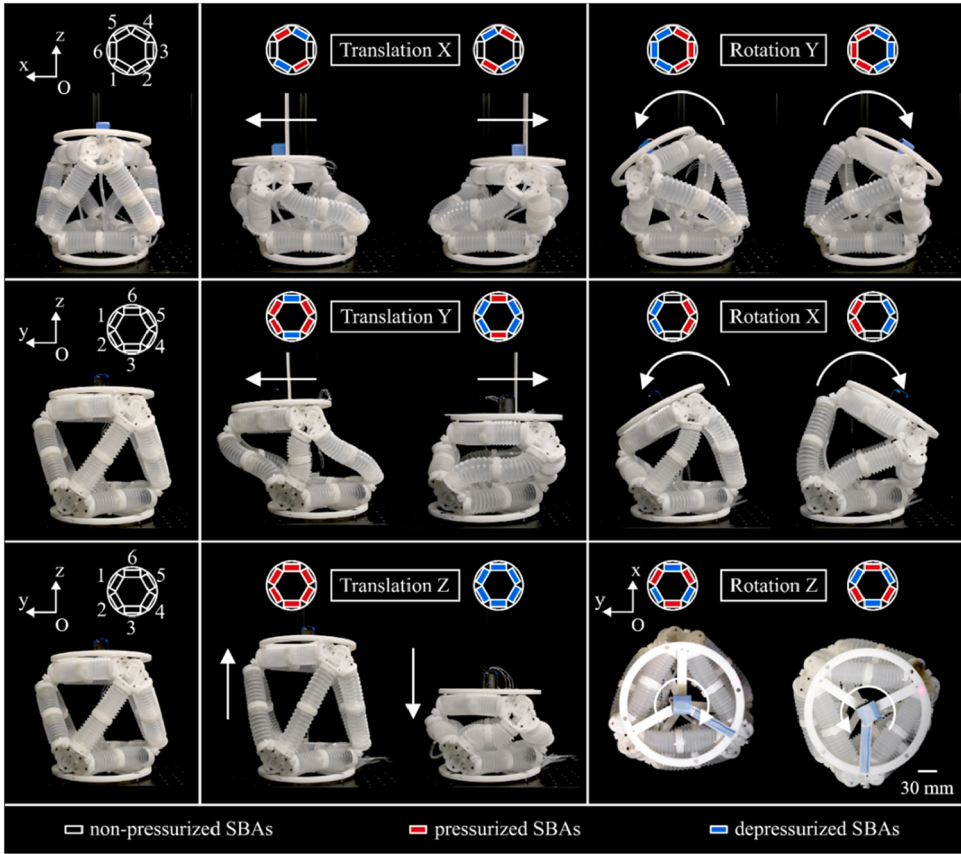


**Fig. 9.** The actuation schemes and movements of the MFA. The circles represent the top view, with six rectangles inside showing the six SBAs of the parallel arm. The blank rectangles indicate no pressure applied, the red rectangles indicate positive pressure, and the blue rectangles indicate negative pressure.

of the SBAs, wherein pneumatic pressure not only contributes to elongation but also resists the forces generated within the coupling. The experiment and model show the best agreement during the extension along the Z-axis. The experimental setup for measuring torque is illustrated in Fig. 10(e), where one end of the torque sensor is connected to a fixed platform, and the other end is attached to the top effector. According to Fig. 10(f), the robot generates torque up to 2.7 Nm.

#### 4.5. Validation of inverse kinematics and control performance

Validating inverse kinematics control is essential for providing controllable motions in real-world applications. This experiment tests the robot's accuracy in reaching target positions and orientations, with a specific focus on coordinated and multi-directional movements. The six-axis inverse kinematics control experiments are conducted using the kinematic evaluation platform. Multi-axis displacement sensors and pressure sensors are added to enable real-time monitoring of the output movements and actuation pressures, respectively. Video tracking markers are introduced to verify the independent control capabilities of each axis and to measure coupling errors between different axes. The recorded video footage is analyzed using an open-source software Tracker. A 20 cm laser reflector plate is used for camera calibration, ensuring precise reference distances and orientation angles.

Considering to counteract coupling forces, a linear compensation is applied to the control pressure in the experiments. The control performance of the six-axis inverse kinematics is validated. Fig. 11(a) illustrates the control outcomes for X, Y, and Z-axis translations. Red, green, and blue represent translations along the X, Y, and Z-axis, respectively. The stars indicate the target points, while the dots represent the reached points, with all marked points located at the center of the top effector. The motion trajectories leading to the target points are also recorded, demonstrating that the control closely follows the desired paths. The experimental data is summarized in Table 4, with the average errors for the three translations being 0.3mm, 2.1mm, and 1.8mm. The control of composite motion in two-axis translation is also tested, as represented by the yellow diamonds. Four target points are set in the four quadrants of the X-Y plane, including three points located at 45° away from X-axis, (-20, 20), (20, -20), (-20, -20), and one point at (10, 30) mm. The actual achieved positions are (-17.8, 23.3), (17.8, -21.0), (-16.9, -20.2), and (15, 32) mm. Although errors increase in composite motions, the overall accuracy remains within acceptable limits, with the error not exceeding a maximum of 3.97 mm.

Fig. 11(b) shows the rotational control results around the X and Y-axis, with green for RX and red for RY. Fig. 11(c) presents the

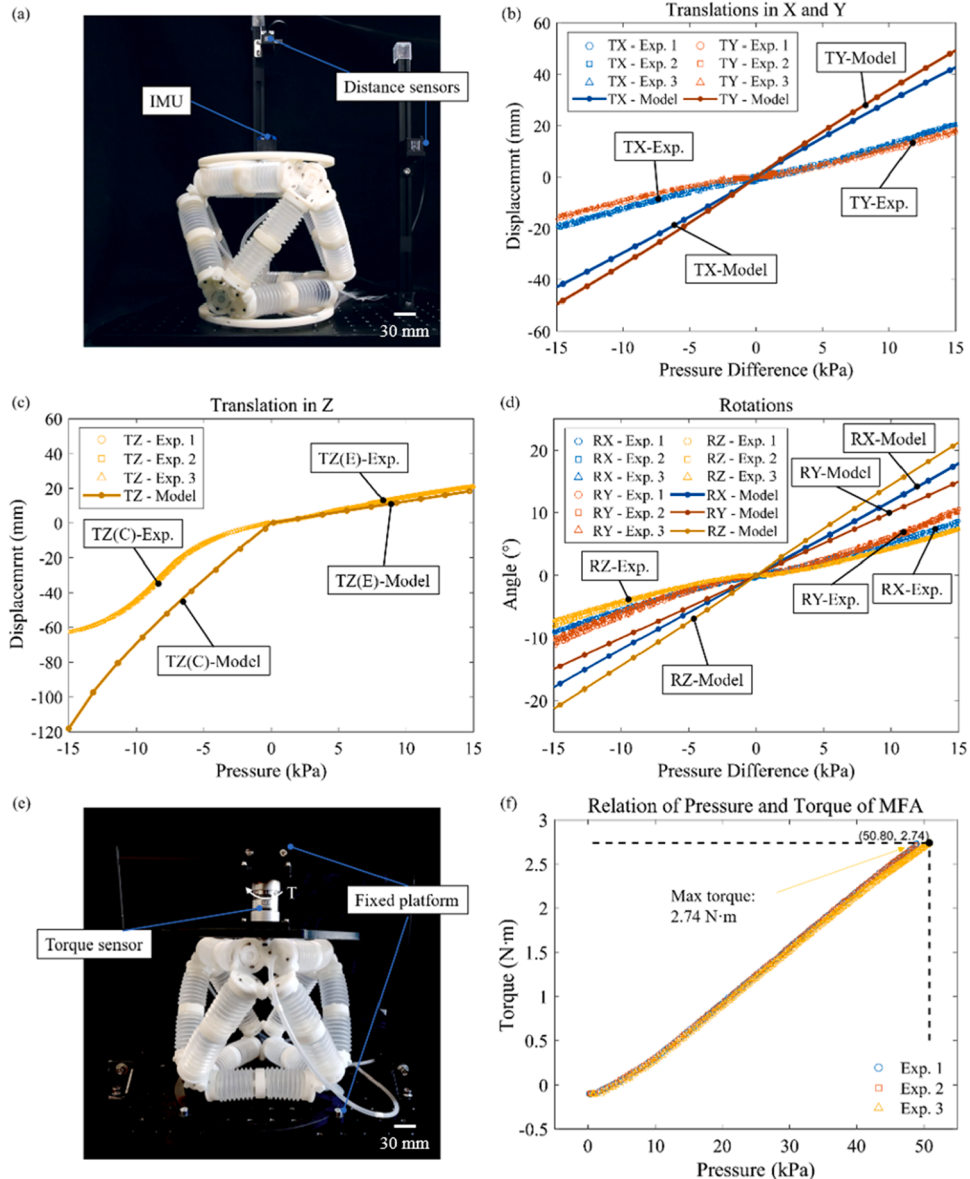


**Fig. 10.** Motion range and forward kinematics validation of the MFA. (a) The experimental setup records rotation angles using an IMU sensor and measures displacements with distance sensors. (b) The pressure-displacement relationship in the X and Y directions, where Exp. and Model denote experimental and model results, respectively. (c) The pressure-displacement relationship in the Z direction indicates the extension and contraction processes with TZ(E) and TZ(C). (d) The pressure-angle relationship in three rotational directions. (e) The torque measurement setup, with the sensor fixed at one end and connected to the robot's top surface at the other. (f) The pressure-torque experiments recorded a maximum torque of 2.74 Nm.

**Table 3**  
Range Of Motions.

Translations	Range	Rotations	Range
X	-43.7 ~ 40.7 mm	X	-28.0 ~ 26.3°
Y	-54.5 ~ 55.1 mm	Y	-29.3 ~ 32.1°
Z	-67.1 ~ 29.4 mm	Z	-35.4 ~ 35.9°

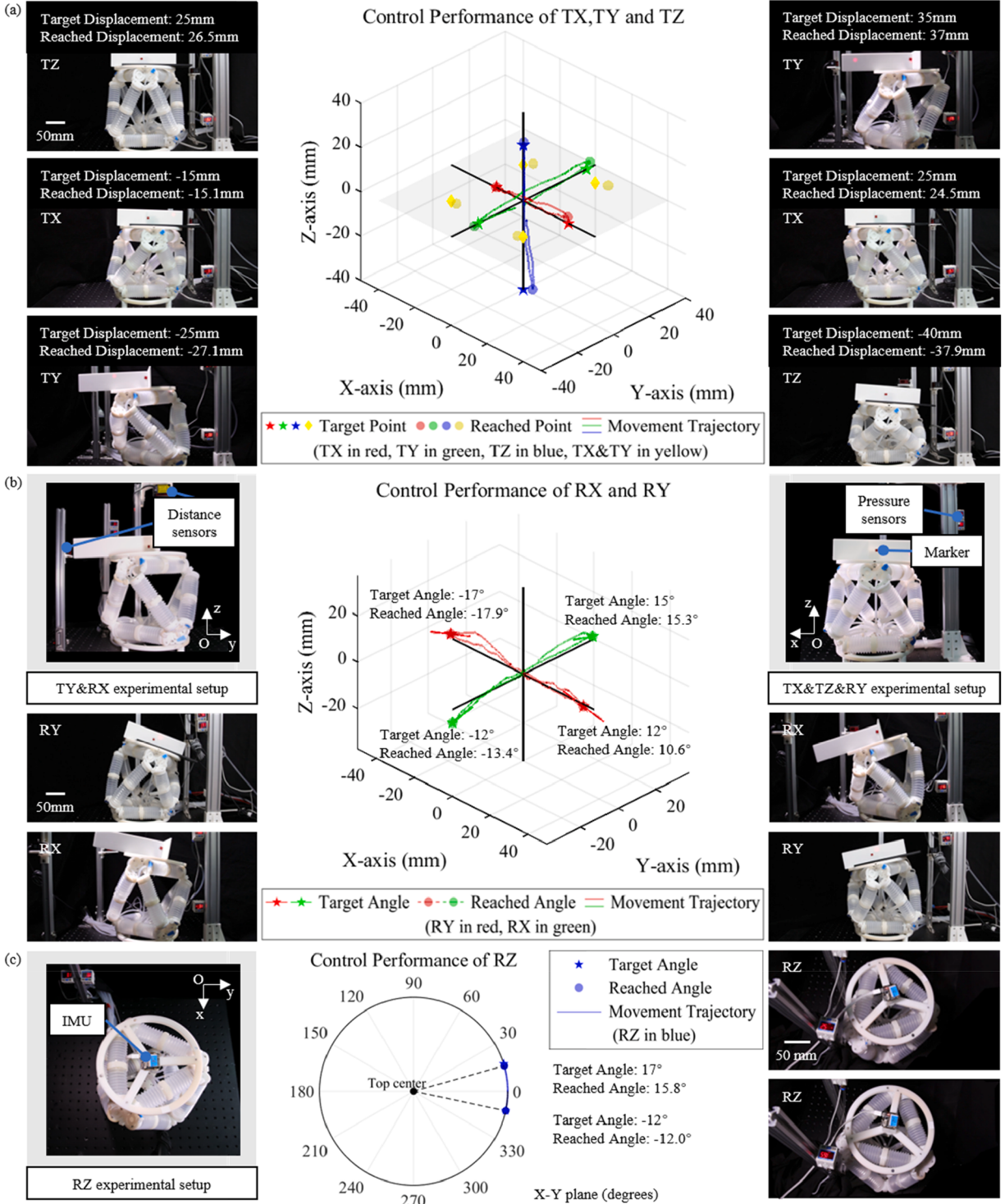


**Fig. 11.** The experimental setup includes an IMU sensor for rotation angles and distance sensors for displacements. Multi-axis displacement and digital pressure sensors display real-time control data, while markers verify the independent control of each axis. (a) Control performance for translations along the X, Y, and Z-axis, with red for TX, green for TY, and blue for TZ. The stars denote target points, and the dots show reached points, along with recorded motion trajectories. (b) Control performance for rotations around the X and Y-axis, with green for RX and red for RY. Target angles, reached angles, and motion trajectories are plotted. (c) Control performance for rotation around the Z-axis, shown in blue from a top-down perspective.

control outcomes for rotation around the Z-axis, represented in blue. The target angles, actual angles, and motion trajectories are plotted, indicating average rotational errors of 0.9°, 1.2°, and 0.6°. Results show the robot's ability to reach to target positions, compensate the coupling, and maintain stability, which together demonstrate the effectiveness of the inverse kinematic model under realistic actuation conditions. Potential sources of control error include model simplification, sensor resolution, fabrication tolerances, and the control strategy. Among these, model simplification is the dominant. The model employs linear fitting, while material's viscoelasticity manifests as hysteresis in loading-unloading cycles, even under quasi-static operations, producing a nonlinear relationship of actuator's performance in practice, which explains the observed RMS errors of 1.6 mm and 0.9° for translation and rotation, respectively. In addition, as the kinematic model does not account for coupling forces, multi-axis motions exhibit larger errors, consistent with the errors observed in composite motion tests.

## 5. Validation of functionality

### 5.1. Narrow space and multi-facet manipulation

As shown in Fig. 12(a), the experiment simulated a comprehensive application scenario designed to test the robot's range of morphing when entering narrow space and multi-facet manipulation ability. The scenario included two acrylic boards placed along the robot's path with a spacing of 170 mm (compared to the robot's width of 230 mm), and three 3D-printed screw nuts and bolts positioned in different orientations in an orthogonal layout. The two acrylic boards simulated the narrow space that the robot needed to traverse before commencing its task. A red bolt is located in the ceiling of the test setup, a blue bolt is on the back side wall, and a green bolt is on the left side wall, requiring the robot to handle overhead and lateral operations. An IMU sensor is mounted on the bolt to monitor changes in rotational angle during the operation.

To show the robot's ability to navigate through narrow environment, the robot passing through the gap between acrylic boards is recorded as illustrated in Fig. 12(b). During the experiment, negative pressure is applied to all actuators, causing the robot to contract to its minimum volume state, with the maximum width reduced to 160 mm. While maintaining this compact state, the robot is pushed forward through the gap until its center aligned with the center of the upper bolt. When the robot reaches the designated position, atmospheric pressure is applied to all actuators to restore the robot to its initial state in preparation for subsequent operations.

The robot performing multi-directional manipulation is presented in Fig. 12(c). In this experiment, the robot is fixed on the experimental platform and tasked with loosening bolts positioned in different directions. To avoid resistance or interference caused by pneumatic tubes during motions, the tubes are bundled and routed with sufficient slack during the experimental setup to ensure a relaxed state throughout the robot's operation. Following a torsional actuation strategy, the robot executed a cyclic sequence of gripper grabbing, arm twisting, gripper releasing, and arm returning by controlling the nearest facet-effector through the coordinated actuation pressures of the SBAs. Fig. 12(d) displays the pressure sensor and IMU sensor data recorded during the process of unscrewing the top bolt. The data captures three twisting actions until the bolt is fully removed. In each twisting action, the gripper's actuator group first applied vacuum to grasp the bolt. Then, the inflation and deflation of the arm actuators operated in an antagonistic manner, collectively generating the twisting motion. The twisting angle increased with the driving pressure until it reached the target value. After unscrewing, the bolt is released and the robot returned to the original state. Although the twisting motion could potentially reduce the overall height of the robot, the gripping effector maintained a firm hold on the bolt, and the passive adaptability of the actuators compensated for this potentially adverse effect.

The robot unscrewed the bolts arranged in an orthogonal layout effectively, demonstrating the excellent multi-facet manipulation capability and adaptability. The robot's rotational range of motion satisfied the requirements for bolt operation. During the releasing and returning process, the robot's working effector may come into contact with the bolt, causing it to rotate in an undesired direction. In real-life applications, this issue can be resolved through more precise pneumatic control. Through multiple iterative steps, the top, front, and left-side effectors precisely unscrewed the bolts in their respective directions, showcasing the robot's ability to handle tasks at multiple orientations without change of position.

### 5.2. Climbing in 3D space

The robot's multi-facet functionality and locomotion ability show application potential in navigating complex environments. For example, the post-disaster rescue missions require robotic system to perform a range of environmental interactions including searching, climbing, traversing rugged terrain, and overcoming obstacles, while minimizing risks to personnel. This requires excellent

**Table 4**

Control Performance.

Transformations	Target 1	Experiment 1	Target 2	Experiment 2	Average error
TX	25 mm	24.5 mm	-15 mm	-15.1 mm	0.3mm
TY	35 mm	37 mm	-25 mm	-27.1 mm	2.1mm
TZ	25 mm	26.5 mm	-40 mm	-37.9 mm	1.8mm
RX	15°	15.3°	-12°	-13.4°	0.9°
RY	12°	10.6°	-17°	-17.9°	1.2°
RZ	17°	15.8°	-12°	-12°	0.6°

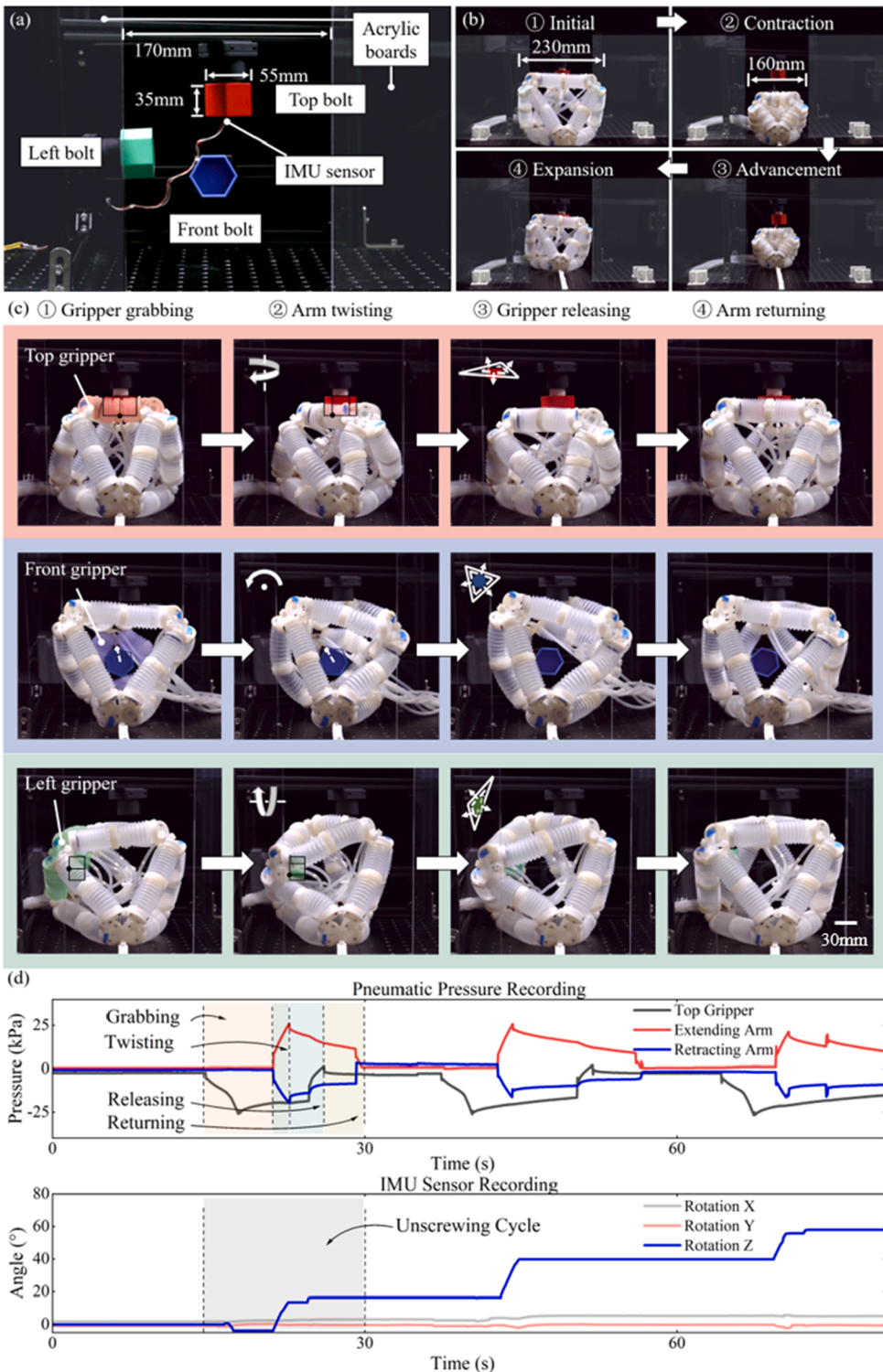


**Fig. 12.** Shrinkage performance and manipulation demonstration of the MFE robot. (a) The experimental setup includes two acrylic boards and three bolts. (b) The motion sequence of the MFE robot passing through the narrow gap by shrinkage deformation. (c) The robot unscrews bolts from distinct orientations through performing a cycle of gripper grabbing, arm twisting, gripper releasing, and arm returning, showcasing its multifaceted manipulation capabilities. (d) The pressure of the SBAs and the angular displacement of the bolt during unscrewing.

mobility, environmental adaptability, and safe interaction. As shown in Fig. 13, a 3D terrain is built to simulate a complex environment with spatially protruding obstacles for the robot to climb and maneuver.

The robot coordinates the actuation pressure of the SBAs based on the translation and rotation-driven strategy, and alternates between expanding and contracting the opposite facet-effectors to grab the anchors, reposition, and move through the anchors. Throughout the process, the robot overcomes the influence of spatial anchors and continuously adjusts its grabbing angle and position to ensure smooth passage. From start to end, the robot performs three grabbing and repositioning maneuvers. In the first step, the robot executed a 45° counter clockwise turn and a 60 mm lateral movement from anchor 1 to 2. The second step involved a 60 mm vertical descent and a 35 mm lateral movement from anchor 2 to 3. The third step consisted of a 45° clockwise turn and another 60 mm lateral movement from anchor 3 to 4. As a result, the robot descends 180 mm from the upper-left starting point anchor 1 to the lower-right endpoint anchor 4, successfully avoiding all obstacles along the way. This process demonstrates the robot's 3D climbing capability utilizing its multi-facet functionality.

### 5.3. Integrated grasping and climbing for object retrieval

By combining its capability of climbing and grasping, the MFE robot is able to finish the object retrieval task as shown in Fig. 14(a). The experimental setup included two fixed anchors positioned at a 120° angle, which were used to reposition the robot during the task. A small ball as the target object is placed on the frame, which can slide horizontally. The ball is connected to a 3D-printed component using magnets. Fig. 14(b) illustrates the motion sequence, the MFE robot first bends, engages the lower gripper to grasp the lower anchor, and the upper gripper releases the upper anchor. Then, the robot uses the lower gripper to firmly hold the base of the anchor. Subsequent translation in the Z and Y directions aligns the upper gripper to hook and guide the ball within easy reach. Finally, fine adjustments of the upper gripper's position and orientation enable a secure grasp of the ball, followed by the arm retraction to place the ball at the designated location. The corresponding control pressure are recorded and plotted in Fig. 14(c). These tasks validate the robot's functions and application potential across various scenarios.

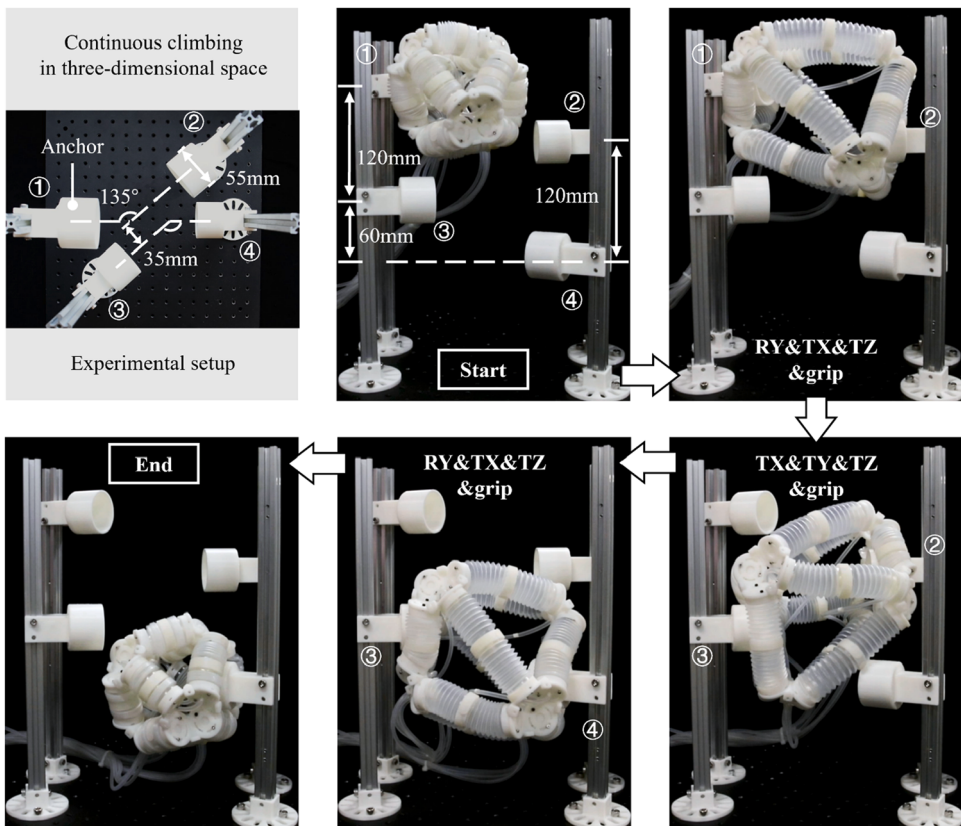


**Fig. 13.** Climbing demonstration of the MFE robot. In a challenging environment with spatially protruding obstacles, the robot achieves 3D climbing in the intricate and interwoven terrains by coordinately adjusting its opposite facet-effectors and alternately expanding and contracting them for grabbing, repositioning, and moving.

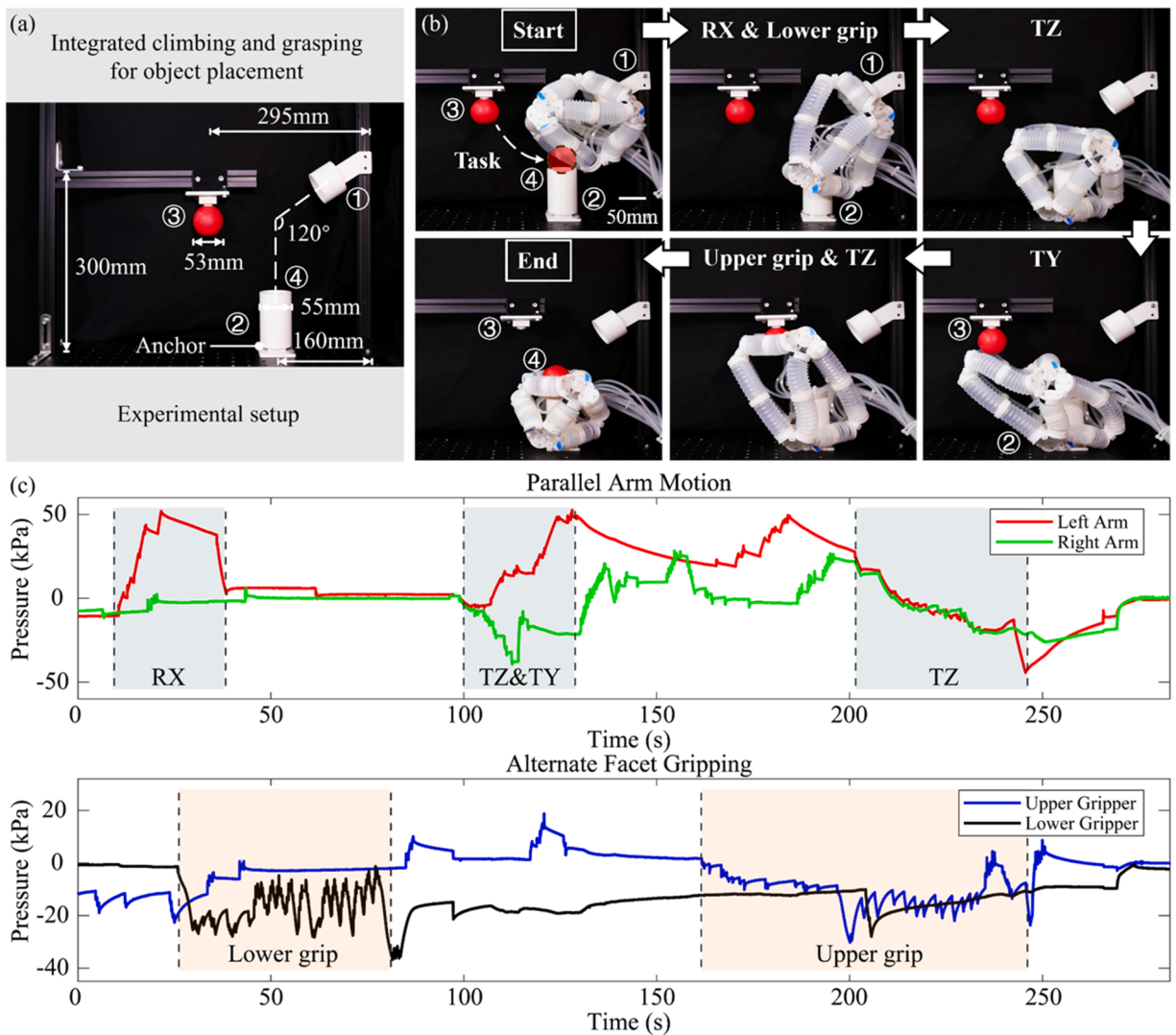


**Fig. 14.** Demonstration of the integrated climbing and grasping capabilities of the MFE robot. (a) The experimental setup includes climbing poles and a small ball that can slide horizontally. (b) The motion sequence of the MFE robot to position the ball accurately at the designated location. (c) The corresponding control pressure during parallel arm motion and alternate facet gripping.

## 6. Conclusion

In this work, a novel approach to design multifunction soft robot is introduced through the implementation of 2D triangular effectors on the discrete surfaces of an octahedral configuration, granting the MFE robot with identical and interchangeable functions of each facet. Each facet of the octahedron possesses the same functional capabilities, thus enabling the multi-faceted effector to exhibit reusability. A systematic topological analysis using the POC equation for the parallel mechanism is conducted, which yields an overall DOF of 6, validating the design. The forward kinematics models are established for USM and CDM forms of the effector. The motion forms enable the MFE robot to carry out tasks involving grasping, locomotion and manipulation functions as the MFG and the MFA. When in the MFG mode, the robot exhibits the capability to grasp objects within a diameter range of 36.3–109.1 mm, with the most significant holding force of approximately 7 N. This gripping capability extends to objects of various shapes, rigidities, and weights. The 6-DOF motions as the MFA are investigated, showing symmetric behavior in 5 DOFs. Translations along the X and Y directions reach approximately 42.2 mm, while translation in the Z direction spans from -67.1 to 29.4 mm. Unidirectional rotation angles around the X, Y, and Z-axis are approximately 27.2°, 30.7°, and 35.7°, respectively.

The inverse kinematics model and control performance of the MFE robot are validated. Experimental results reveal average errors of 0.3 mm, 2.1 mm, and 1.8 mm in translational control across the three axes, and 0.9°, 1.2°, and 0.6° in rotational control. Building on the validated motion control, scenario-specific experiments are conducted to demonstrate the robot's functionalities, including navigation through narrow spaces, multidirectional object manipulation in confined environments, 3D climbing on complex terrains, and

efficient object retrieval through integrated grasping and locomotion.

The work's advantages lie in the design and multidirectional function reuse, showcasing a balanced performance in both grasping and motion functions. The repetitive-facet configuration allows for identical motion and functionality across each facet, enabling the achievement of versatile capabilities without the need for intricate and specific designs. The research holds potential contributions to the development of soft robots for multifunctional applications in unstructured environments.

Despite demonstrating six-DOF motion and multifunctionality, the current system faces some limitations. Future work may focus on developing compact or untethered pneumatic systems, enabling deployment in confined or field environments. Coordinated deformation across adjacent facets may further expand the robot's manipulation range. Additionally, feedback can be incorporated into the motion model to account for hysteresis, creep, and nonlinear dynamic characteristics, in order to improve control accuracy. Furthermore, enhancing actuation speed through control optimization and real-time feedback integration could improve system responsiveness and reliability.

#### CRediT authorship contribution statement

**Yige Wu:** Writing – original draft, Visualization, Validation, Methodology, Investigation, Formal analysis, Data curation, Conceptualization. **Nan Huang:** Visualization, Software, Methodology, Investigation, Formal analysis, Data curation. **Shaowu Tang:** Visualization, Validation, Software, Investigation. **Xiaohuang Liu:** Visualization, Investigation. **Xianxu Li:** Investigation. **Sicong Liu:** Writing – review & editing, Supervision, Project administration, Investigation, Funding acquisition, Formal analysis, Conceptualization. **Juan Yi:** Writing – review & editing. **Zheng Wang:** Writing – review & editing, Funding acquisition. **Jian S Dai:** Writing – review & editing.

#### Declaration of competing interest

The authors declare that they have no known competing financial interests or personal relationships that could have appeared to influence the work reported in this paper.

#### Acknowledgements

This work was partly supported by the National Natural Science Foundation of China under Grant 52475302 and 52335003, National Key R&D Program of China (Grant No. 2022YFB4701200), Shenzhen Science and Technology Program Grant JCYJ20220530114615034 and JCYJ20220818100417038, Guangdong Provincial Key Laboratory of Intelligent Morphing Mechanisms and Adaptive Robotics under Grant 2023B1212010005.

#### Supplementary materials

Supplementary material associated with this article can be found, in the online version, at [doi:10.1016/j.mechmachtheory.2025.106240](https://doi.org/10.1016/j.mechmachtheory.2025.106240).

#### Data availability

All the data are included in the manuscript and supplementary files.

#### References

- [1] O. Yasa, Y. Toshimitsu, M.Y. Michelis, et al., An Overview of Soft Robotics, *Annual Review of Control, Robotics, and Autonomous Systems* 6 (1) (2023) 1–29.
- [2] D. Rus, M.T. Tolley, Design, fabrication and control of soft robots, *Nature* 521 (7553) (2015) 467–475.
- [3] Xiaoqian Chen, et al., A review of soft manipulator research, applications, and opportunities, *Journal of Field Robotics* 39 (2022) 281–311, 3.
- [4] P. Polygerinos, Z. Wang, K.C. Galloway, R.J. Wood, C.J. Walsh, Soft robotic glove for combined assistance and at-home rehabilitation, *Robotics and Autonomous Systems* 73 (2015) 135–143.
- [5] S. Liu, Y. Zhu, Z. Zhang, et al., Otariidae-Inspired Soft-Robotic Supernumerary Flippers by Fabric Kirigami and Origami, *IEEE/ASME Transactions on Mechatronics* 26 (5) (2021) 2747–2757.
- [6] Kailuan Tang, et al., A Strong Underwater Soft Manipulator with Planarly-bundled Actuators and Accurate Position Control, *IEEE Robotics and Automation Letters* (2023).
- [7] M. Calisti, G. Picardi, C. Laschi, Fundamentals of soft robot locomotion[J], *Journal of The Royal Society Interface* 14 (130) (2017) 20170101.
- [8] J. Yi, X. Chen, C. Song, et al., Customizable three-dimensional-printed origami soft robotic joint with effective behavior shaping for safe interactions[J], *IEEE Transactions on Robotics* 35 (1) (2018) 114–123.
- [9] J. Shintake, V. Cacucciolo, D. Floreano, H. Shea, Soft Robotic Grippers, *Advanced Materials* 30 (29) (2018) 1707035.
- [10] Salerno, Marco, et al. "A novel 4-DOFs origami enabled, SMA actuated, robotic end-effector for minimally invasive surgery." 2014 IEEE international conference on robotics and automation (ICRA). IEEE, 2014.
- [11] J. Fang, Y. Zhuang, K. Liu, et al., A Shift from Efficiency to Adaptability: Recent Progress in Biomimetic Interactive Soft Robotics in Wet Environments, *Advanced Science* 9 (8) (2022) 2104347.
- [12] L. Zhou, L. Ren, Y. Chen, S. Niu, Z. Han, L. Ren, Bio-Inspired Soft Grippers Based on Impactive Gripping", *Advanced Science* 8 (9) (2021) 2002017.
- [13] Zheng Wang, et al., The next-generation surgical robots, *Surgical Robotics* (2018) 1.

- [14] J. Yang, C. Ren, C. Yang, et al., Design of a flexible capture mechanism inspired by sea anemone for non-cooperative targets[J], Chinese Journal of Mechanical Engineering 34 (1) (2021) 77.
- [15] R. Baines, S K Patiballa, J. Booth, et al., Multi-environment robotic transitions through adaptive morphogenesis[J], Nature 610 (7931) (2022) 283–289.
- [16] Q. Liu, X. Gu, N. Tan, H. Ren, Soft Robotic Gripper Driven by Flexible Shafts for Simultaneous Grasping and In-Hand Cap Manipulation, IEEE Transactions on Automation Science and Engineering 18 (3) (2021) 1134–1143.
- [17] Z. Xie, F. Yuan, J. Liu, et al., Octopus-inspired sensorized soft arm for environmental interaction, Science Robotics 8 (84) (2023) eadh7852.
- [18] K. Nakajima, H. Hauser, R. Kang, et al., A soft body as a reservoir: case studies in a dynamic model of octopus-inspired soft robotic arm[J], Frontiers in computational neuroscience 7 (2013) 91.
- [19] Jian S. Dai, Matteo Zoppi, in: Xianwen Kong (Ed.), Advances in reconfigurable mechanisms and robots I, Springer, London, 2012.
- [20] F. Aimeedee, et al., Systematization of morphing in reconfigurable mechanisms, Mechanism and machine theory 96 (2016) 215–224.
- [21] D.S. Shah, J.P. Powers, L.G. Tilton, S. Kriegman, J. Bongard, R. Kramer-Bottiglio, A soft robot that adapts to environments through shape change, Nature Machine Intelligence 3 (1) (2021) 51–59.
- [22] Qinlin Tan, et al., Underwater crawling robot with hydraulic soft actuators, Frontiers in Robotics and AI 8 (2021) 688697.
- [23] D. Xie, J. Liu, R. Kang, et al., Fully 3D-printed modular pipe-climbing robot[J], IEEE Robotics and Automation Letters 6 (2) (2020) 462–469.
- [24] Singh, G., S. Patiballa, X. Zhang, and G. Krishnan, “A Pipe-Climbing Soft Robot”, 2019 International Conference on Robotics and Automation (ICRA), (2019), 8450–8456.
- [25] S. Liu, J. Liu, K. Zou, et al., A Six Degrees-of-Freedom Soft Robotic Joint With Tilt-Arranged Origami Actuator, Journal of Mechanisms and Robotics 14 (060912) (2022).
- [26] Jianhui Liu, et al., Vertebral Soft Robotic Joint Design With Twisting and Antagonism, IEEE Robotics and Automation Letters 7 (2021) 658–665, 2.
- [27] W. Kim, J. Byun, J K Kim, et al., Bioinspired dual-morphing stretchable origami[J], Science robotics 4 (36) (2019) eaay3493.
- [28] M. Feng, D. Yang, L. Ren, et al., X-crossing pneumatic artificial muscles[J], Science Advances 9 (38) (2023) eadi7133.
- [29] R. Zhu, D. Fan, W. Wu, et al., Soft robots for cluttered environments based on origami anisotropic stiffness structure (OASS) inspired by desert iguana[J], Advanced Intelligent Systems 5 (6) (2023) 2200301.
- [30] D. Li, D. Fan, R. Zhu, et al., Origami-inspired soft twisting actuator[J], Soft Robotics 10 (2) (2023) 395–409.
- [31] Z. Jiao, C. Zhang, W. Wang, et al., Advanced artificial muscle for flexible material-based reconfigurable soft robots[J], Advanced Science 6 (21) (2019) 1901371.
- [32] J. Sun, E. Lerner, B. Tighe, et al., Embedded shape morphing for morphologically adaptive robots[J], Nature Communications 14 (1) (2023) 6023.
- [33] A. Yin, H.-C. Lin, J. Thelen, B. Mahner, T. Ranzani, Combining Locomotion and Grasping Functionalities in Soft Robots, Advanced Intelligent Systems 1 (8) (2019) 1900089.
- [34] M. Cianchetti, M. Calisti, L. Margheri, M. Kuba, C. Laschi, Bioinspired locomotion and grasping in water: the soft eight-arm OCTOPUS robot, Bioinspiration & Biomimetics 10 (3) (2015) 035003.
- [35] Liu, Sicong, et al. “Deployable prismatic structures with origami patterns.” International Design Engineering Technical Conferences and Computers and Information in Engineering Conference. Vol. 46377. American Society of Mechanical Engineers, 2014.
- [36] Zhonggui Fang, et al., Omnidirectional compliance on cross-linked actuator coordination enables simultaneous multi-functions of soft modular robots, Scientific Reports 13 (2023) 12116, 1.
- [37] Peter Wharton, et al., Tetraflex: A Multigait Soft Robot for Object Transportation in Confined Environments, IEEE Robotics and Automation Letters (2023).
- [38] Q. Guan, L. Liu, J. Sun, et al., Multifunctional Soft Stackable Robots by Netting–Rolling–Splicing Pneumatic Artificial Muscles, Soft Robotics 10 (5) (2023) 1001–1014.
- [39] N.S. Usevitch, Z.M. Hammond, M. Schwager, A.M. Okamura, E.W. Hawkes, S. Follmer, An untethered isoperimetric soft robot, Science Robotics 5 (40) (2020) eaaz0492.
- [40] J. Zhou, Y. Chen, X. Chen, et al., A proprioceptive bellows (PB) actuator with position feedback and force estimation[J], IEEE Robotics and Automation Letters 5 (2) (2020) 1867–1874.
- [41] Xiaojiao Chen, Yaixin Guo, Dehao Duanmu, Jianshu Zhou, Wei Zhang, Zheng Wang, Design and modeling of an extensible soft robotic arm, IEEE Robotics and Automation Letters 4 (4) (2019) 4208–4215.
- [42] S. Wang, X. Yang, Y. Chen, et al., A theoretical design of a bellow-shaped statically balanced compliant mechanism[J], Mechanism and Machine Theory 161 (2021) 104295.
- [43] Wei-Hang Tian, et al., Development of a tetrahedral-shaped soft robot arm as a wrist rehabilitation device using extension type flexible pneumatic actuators, Journal of Robotics and Mechatronics 32 (2020) 931–938, 5.
- [44] Ziming Zhao, et al., Envelop-Climbing Locomotion Planning and Capability Analysis of a Deformable Tetrahedron Rolling Robot, IEEE Robotics and Automation Letters (2023).
- [45] H. Shang, D. Wei, R. Kang, et al., Gait analysis and control of a deployable robot[J], Mechanism and machine theory 120 (2018) 107–119.
- [46] J.C. Zagal, C. Armstrong, S. Li, Deformable Octahedron Burrowing Robot (2012).
- [47] J. Cui, P. Wang, T. Sun, et al., Design and experiments of a novel quadruped robot with tensegrity legs[J], Mechanism and Machine Theory 171 (2022) 104781.
- [48] F. Aimeedee, G. Gogu, J S Dai, et al., Systematization of morphing in reconfigurable mechanisms[J], Mechanism and machine theory 96 (2016) 215–224.
- [49] Advances in reconfigurable mechanisms and robots I[M]. London: Springer, 2012.
- [50] T L Yang, A. Liu, H. Shen, et al., Topology design of robot mechanisms[M], Springer, Singapore, 2018.
- [51] Faye Y. Wu, H. Harry Asada, Implicit and intuitive grasp posture control for wearable robotic fingers: A data-driven method using partial least squares, IEEE Transactions on Robotics 32 (2016) 176–186, 1.
- [52] Li, Shuguang, et al. “A vacuum-driven origami ‘magic-ball’ soft gripper.” 2019 International Conference on Robotics and Automation (ICRA). IEEE, 2019.